ICARUS **123,** 129–167 (1996)
ARTICLE NO. 0146

The Dynamics of the Neptunian Adams Ring's Arcs

DIETMAR W. FORYTA*

Observatoire de Paris, DAEC-EUROPA, 92195 Meudon Cédex Principal, France

AND

BRUNO SICARDY

Observatoire de Paris, DESPA, Institut Universitaire de France, Paris 6, 92195 Meudon Cédex Principal, France
E-mail: sicardy@mesiob.obspm.fr

Received October 11, 1995; revised April 1, 1996

We examine the resonant forcing of a narrow ringlet by a nearby satellite on an inclined, but circular, orbit. The general techniques that we develop are used to study the dynamics of Neptune's ring arcs, near the 43:42 mean motion resonances with the satellite Galatea. More specifically, the averaged equations of motions are used to analyze the coupling between the various resonances at work, while a mapping integrator allows us to integrate the motion of up to 10^4 particles for several centuries. We show that even in the absence of dissipation, the coupling between the horizontal and vertical motions of the particles can lead to a stochastic migration of the particles for one to the other of the $43 \times 2 = 86$ corotation sites where the arcs are assumed to be trapped. The pressure of solar radiation sweeps out from the arcs the particles with a ratio $\beta_\odot$ of pressure of radiation to solar gravitation larger than ~ 0.01, corresponding to ~ 50 μm-sized icy particles in the limit of geometrical optics. Poynting–Robertson (PR) drag, on the other hand, has only a small effect on dust particles *already* inside the corotation sites. In contrast, PR drag rapidly drives the particles lying outside these sites on unstable orbits. Inelastic collisions between the larger particles remain the most serious problem for the arc stability. We discuss the implications of these results in terms of a population of large particles being the source of dusty arcs. We show in particular that such structures, while not permanent, can be nevertheless statistically common at corotation resonances with a nearby satellite such as Galatea.

1. INTRODUCTION

Both ground-based and space observations have shown in the last two decades that planetary rings present not only fine radial structures, but also complex azimuthal and vertical features: wakes, kinks, braids, arcs, spokes, etc. Although the spatial extents of these structures remain small compared to the global dimensions of the rings, they are nevertheless interesting because they are clues of ongoing processes in these evolving systems.

We focus in this paper on a detailed analysis of the dynamics of Neptune's arcs. Although arc structures have been detected in other ring systems, Neptune's arcs occupy for the moment a unique position. In effect, both ground-based and *Voyager* observations provide us with accurate measurements of their mean motion, physical width, azimuthal extension, radial distortion, optical depth, etc. Also, precise locations of the resonances associated with the nearby satellite Galatea can now be derived from the *Voyager* results (see Section 2).

Numerical simulations have tested the various analytical models proposed to explain the arc stability, but they had to use scaling factors in order to avoid vanishingly small perturbing terms, and thus, unacceptably long computer runs. Our purpose here is to study the effect of a small satellite on a narrow ringlet, using the *real* parameters of the system. We have derived two methods for that.

First, we write the *averaged equations of motion* near an $m + 1{:}m$ mean motion resonance. These equations keep only the resonant terms arising from the satellite potential (plus the secular terms caused by the planet's oblateness). Up to three resonant arguments, associated with the particle orbital eccentricity and inclination and with the satellite inclination, couple together, describing the complex 3-D motion of a particle near the $m + 1{:}m$ resonance. The advantage of this method is to allow a better insight of the global dynamics of the arcs, through classical methods of study of dynamical systems, like surfaces of section. Moreover, the equations are written in nondimensional units, so that applications to other ringlets

* Present address: Universidade Federal do Paraná, Dpto de Física, Centro Politécnico, CP 19081, 81531-990 Curitiba, Paraná, Brazil. E-mail: foryta@fisica.ufpr.br.

0019-1035/96 $18.00

can easily be considered by just changing a few numerical coefficients.

In a second approach, we use a *3-D mapping integrator*. The mapping assumes that the orbital (epicyclic) elements of a particle are instantaneously changed at each conjunction with the satellite. It yields the new elements as a function of the old ones. The advantage of the mapping is that it is very fast and allows us to follow up to 10^4 particles having up to 10^4 conjunctions with the perturbing satellite. Again, the mapping is written in nondimensional units and can thus be implemented in any configuration where a ringlet is perturbed by one or more satellites. The mapping must reproduce both the high-frequency terms arising from individual conjunctions, and the low-frequency terms associated with possible resonances.

The two methods outlined above are described in appendixes, which can be read independently in a quite general context. Also, more details on some technical aspects of this paper can be found in their original form in Foryta (1993).

The main body of this article is devoted to Neptune's ring arcs. Section 2 gives an overview of the problem. Section 3 presents the averaged equations of motion near the 42:43 resonance with Galatea. The basic frequencies entering in the motion of the arcs are calculated in Section 4. The couplings between the various resonant arguments, and the origin of the possible chaoticity of the arc motion are examined in Section 5. Section 6 presents the mapping method, and Section 7 makes use of it to describe the stochastic migration of some arc particles from site to site. The effects of radiation forces are investigated in Section 8 and collisions are discussed in Section 9. Section 10 presents a discussion and concluding remarks.

2. OVERVIEW

A brief summary of the main physical and dynamical properties of Neptune's arcs are given in this section. More complete reviews can be found in Lissauer and Nicholson (1990), Sicardy and Lissauer (1992), Goldreich (1992), as well as in the comprehensive chapter by Porco *et al.* (1995), and in the references therein.

2.1. Physical Properties of Neptune's Arcs

Neptune's ring arcs were first discovered from the ground in 1984, during a campaign of observations of stellar occultations by the planet and its surroundings (Hubbard *et al.* 1986; Sicardy *et al.* 1991). Subsequent observations showed intermittent evidence for material around Neptune (Covault *et al.* 1986; Nicholson *et al.* 1990, 1995). Everything considered, the frequency of ground-based detections implies that the azimuthal coverage of the ring arc material is about 10% of the total orbit during the 1980 decade.

These detections were confirmed and complemented by the *Voyager* observations, during its flyby of Neptune in August 1989. The *Voyager* mission brought a wealth of information on the neptunian ring system. The three main arcs detected by the spacecraft, Liberté, Egalité and Fraternité, in order of increasing longitude, share the same orbit at 62,932 km from the planet center. These three features span respectively 4°, 4°, and 10° in longitude at half-maximum and have roughly the same brightness. They are preceded by a smaller arc, Courage, which spans 2° or so and is about three times fainter than the main arcs. All of these structures are embedded in a continuous ring (Adams) about 10 times fainter than the main arcs. From a more global point of view, the arc region appears as a relatively compact interval of $\sim 40°$ in longitude, containing denser material, while the continuous Adams ring reaches a minimum of brightness 180° away from the arc region (Showalter and Cuzzi 1992).

The physical width W of the arcs (resolved during ground-based stellar occultations) is typically 15 km, while the optical depth τ lies in the range 0.05–0.08, depending on the event (Nicholson *et al.* 1990, Sicardy *et al.* 1991). Both ground-based and *Voyager* observations give a typical equivalent width (optical depth $\times$ physical width) of ~ 1 km for the arcs, and less than 0.1 km for the continuous part of Adams ring. The photometric properties of the ring and the arcs suggest (although not unequivocally) a significant presence of dust particles both in the arcs and in the ring (Ferrari and Brahic 1994, Porco *et al.* 1995). No individual moonlet has been so far detected inside Adams ring, down to a limit of about 10 km in diameter (Smith *et al.* 1989). However, clumps of material with a typical length of 500–1000 km are observed in the highest resolution images of the arcs. Moreover, no arc structures have been clearly identified in any of the Neptune rings other than Adams.

2.2. Dynamical Problems

If it were only for the Keplerian differential motion, particles with semi-major axes differing by Δa would spread at an angular rate of $d(\Delta\theta)/dt = 3/2\,(\Delta a/a)n$, where n is the mean motion. If Δa were equal to the observed physical width, say $W \sim 15$ km, each of Neptune's arcs should disappear, as individual structures, in a matter of weeks. In any case, it would take an initially condensed arc less than four years to form a roughly uniform ring around the planet. In contrast, the ground-based observations, combined to the *Voyager* data indicate that the arcs are stable over a period of at least five years.

More precisely, these observations are consistent with the three main arcs having a common orbit with two possible mean motions n, confined in very narrow intervals: $n = 820.1194° \pm 0.0006°\ \text{day}^{-1}$ or $820.1118° \pm 0.0006°\ \text{day}^{-1}$

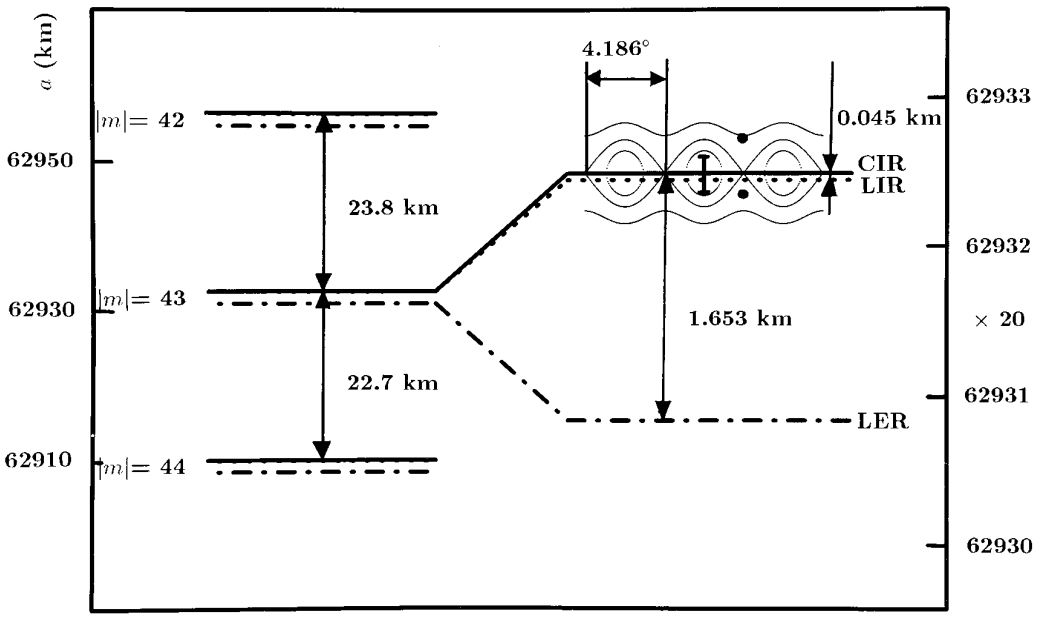

FIG. 1. Radii of three mean motion resonances $m{:}m + 1$ with Galatea. $|m| = 43$ means that the particle completes 42 orbits when the satellite completes 43. The slight splitting of the resonances with a same m is caused by the oblateness of the planet. On the right of the figure, the radial scale has been expanded by a factor 20 to better show the splitting between the three resonances CIR, LIR, and LER (see the Section 3 for the nomenclature used here). The vertical error bar on the CIR radius shows the uncertainty on the resonance locations. The two dots just right of the error bar show the two possible geometrical radii of the arcs, as derived from their expected mean motion. The internal uncertainty attached to those radii is comparable to the size of the dots (see the text and Nicholson *et al.* 1990, 1995). A few trajectories of particles' guiding centers near the corotation sites are overlaid on top of the CIR radius. They illustrate the expected sites' widths (~0.5 km), using the nominal orbital inclination of Galatea (0.0544°). The longitudinal extension $4.186° = 360°/2|m|$ represents the regular partitioning of the corotation sites around the planet.

(Nicholson *et al.* 1990, 1995; Porco *et al.* 1995). Interestingly enough, these two possible mean motions place the arcs very near the mean motion resonance 42:43 with the satellite Galatea, the latter completing 43 revolutions while the arcs complete 42 revolutions (see Fig. 1, Porco 1991, and the discussion in Section 3).

Resonance trapping has actually been invoked shortly after Neptune's arcs discovery to explain their azimuthal confinement. In Lissauer's model (1985), the stable Lagrange points L_4 and L_5 due to a moonlet sharing the arc orbit would ensure the azimuthal confinement, while a second satellite provides the energy the arcs lose through inelastic collisions. Another model, developed by Goldreich *et al.* (1986), requires only one satellite which creates at the same time the "corotation resonances" where the arcs can be confined, and the "Lindblad resonances" which provide the particles the energy they dissipate through collisions (see Section 3 for the nomenclature). Both mechanisms were successfully tested in numerical simulations by Lin *et al.* (1987) and by Sicardy (1991).

The work of Porco (1991) pleads in favor of Goldreich *et al.*'s model in the sense that the mean motion of the arcs places them right on top of the 42:43 *corotation inclined resonance* with Galatea, see Fig. 1. Note in this diagram the very small error bars associated with the radius of the arcs as derived from their mean motion. In particular, a fortuitous coincidence of the arc semi-major axis and the corotation resonance radius can be ruled out with a probability of ~99%, considering (i) the typical spacing between successive corotation resonances (~23 km) and (ii) the error bars attached to the various radii plotted in Fig. 1.

Another point in favor of the 42:43 corotation resonance model is the forced eccentricity expected from the proximity of the 42:43 *Lindblad resonance*. The forced value is proportional to the inverse of the distance between the arc semi-major axis and the Lindblad resonance radius (i.e., about 1.65 km in our case, see Fig. 1), and is directly proportional to the mass of the satellite, see Eq. (13). If due to a resonant forcing, the observed arc eccentricity provides an estimation of Galatea's mass ($2.12 \pm 0.21 \times 10^{21}$ g) and density $\rho = 1.0 \pm 0.5$ g cm^{-3} (Porco 1991, Porco *et al.* 1995). The latter value is quite reasonable for a small icy satellite.

Finally, the *phase* of the radial distorsion with respect to the satellite also argues in favor of a resonant driving, as opposed to a mere wake forced by a single encounter with Galatea (Porco *et al.* 1995). More specifically, the 42-lobed radial distorsion detected in the arcs is such that a given particle is at apocenter (farther away from Galatea) at the conjunction with the satellite, see Fig. 14.

Although a general picture of Neptune's arcs seems to emerge from the previous model, several problems are still unresolved in this corotation resonance model (see also Porco 1991 and Porco *et al.* 1995). Among them, we note that:

• The azimuthal extensions of the arcs should be consistent with a regular partitioning of Adams ring in $43 \times 2 = 86$ corotation sites, spanning each $360°/86 \sim 4.18°$. This is roughly correct for Liberté and Egalité, but Fraternité is then sitting on top of three sites, an *a priori* quite unstable situation. Moreover, the arcs are concentrated in a relatively narrow azimuthal range, a nonrandom distribution which requires explanation.

• The estimated mass of Galatea, combined to its measured orbital inclination, yields the spread of semi-major axes for which the particles are trapped in corotation sites (Eq. (9)). The derived value, about 0.5 km, is substantially smaller than the actual physical width $W \sim 15$ km. This requires a strong eccentricity gradient across the arc, resulting in uncomfortably high relative velocities (and thus large dissipation rate) between colliding particles.

To resolve these apparent contradictions, we must go through a detailed analysis of each step leading to the corotation resonance model. First, we will show that a test particle at a mean motion resonance exhibits a surprisingly complex behavior. This is due to nonlinear couplings between various resonant terms overlapping in a small interval (Fig. 1). For certain initial conditions, a stochastic motion from site to site is possible, even without any dissipative forces or collisions being introduced. Second, nongravitational processes (radiation forces, Poynting–Robertson drag or collisions) are quite important and act on particles of quite different sizes. It is our aim in this paper to address these questions. We certainly cannot be exhaustive in our analysis, owing to the complexity of the various phenomena entering in this problem. We think, however, that these steps must be quantitatively discussed before any conclusion be derived as to the arc origin and evolution.

3. DYNAMICAL STRUCTURE OF THE PROBLEM: THE AVERAGED EQUATIONS

Henceforth, a, e, I, Ω and ϖ denote the usual Keplerian elements: semi-major axis, eccentricity, inclination, longitude of the node, longitude of the periapse. The quantities n and λ denote the mean motion and the mean longitude, respectively, and the subscript s refers to the perturbing satellite Galatea. The main dynamical parameters of the arcs and Galatea are summarized in Table I.

Let us consider a first-order mean motion resonance $m + 1{:}m$ (m integer) between the satellite and a ring particle. This corresponds to $(m + 1)n_s - mn \ll n$; i.e. the angle $(m + 1)\lambda_s - m\lambda$ is almost stationary. We examine for the moment the *average* effect of such a commensurability. We thus ignore, in this section at least, the high-frequency terms arising from the conjunctions with the satellite. Also, we ignore for the moment the effects of other nearby resonances, corresponding to different m's.

TABLE I
Dynamical Parameters of Neptune's Arcs

Neptune mass[a], GM_N	6835107.0 ± 15 km^3 sec^{-1}
Neptune equatorial radius[a]	25225 km
Neptune second zonal coefficient[a], J_2	$(341.05 \pm 0.9)\times10^{-5}$
Neptune fourth zonal coefficient[a], J_4	$(-3.47\pm 0.1)\times10^{-5}$
Galatea mass[b]	2.12×10^{21} g
Galatea mean motion[a]	839.6598 ± 0.0025 deg./day
Galatea orbital mean radius[a]	61952.67 ± 0.13 km
Galatea orbital eccentricity[a]	$(0.120 \pm 0.149)\times10^{-3}$
Galatea orbital inclination[a]	0.0544 ± 0.0132 deg.
Preferred arc mean motion[c]	820.1194 ± 0.0006 deg./day

[a] From Owen *et al.*, 1991
[b] From Porco *et al.*, 1995
[c] From Nicholson *et al.*, 1995

Near the resonance radius, the perturbing function R acting on the particle contains in principle four kinds of trigonometric terms, with four slowly variable arguments Ψ (see Appendix A). These four resonant arguments Ψ are obtained by substracting ϖ, ϖ_s, Ω and Ω_s from $(m + 1)\lambda_s - m\lambda$ (see Table II). The amplitude of these trigonometric terms are respectively proportional to the orbital eccentricities e and e_s of the particle and the satellite, and to the square of the orbital inclinations I and I_s of these two objects.

Each of the angles Ψ_{CE}, Ψ_{LE}, Ψ_{LI}, Ψ_{CI} of Table II describes a resonance, referred to as:

• the corotation inclined resonance (CIR), associated with Ψ_{CI},
• the Lindblad eccentric resonance (LER), associated with Ψ_{LE},
• the Lindblad inclined resonance (LIR), associated with Ψ_{LI}, and
• the corotation eccentric resonance (CER), associated with Ψ_{CE}.

The perturbing function R contains furthermore the secular terms due to the planet's oblateness. Only terms in J_2 are considered in R. Terms in J_4 would unnecessarily complicate the equations without bringing more information. However, in the calculation of the absolute resonance radii, the terms in J_4 have also been included (Eqs. A6), in order to be consistent with other authors, and also with the accuracy now reached on the arc geometrical radius (Porco 1991, Porco *et al.* 1995). We do *not* take into account

TABLE II
Resonance Nomenclature and Locations

Resonance	Critical angle	Geometrical radius[a] for $m = -43$ (km)
Corotation Inclined (CIR)	$\Psi_{CI} = 2[(m+1)\lambda_s - m\lambda - \Omega_s]$	$a_{CI} = 62932.492 \pm 0.124$
Lindblad Eccentric (LER)	$\Psi_{LE} = (m+1)\lambda_s - m\lambda - \varpi$	$a_{LE} = 62930.839 \pm 0.124$
Linblad Inclined (LIR)	$\Psi_{LI} = 2[(m+1)\lambda_s - m\lambda - \Omega]$	$a_{LI} = 62932.447 \pm 0.124$
Corotation Eccentric (CER)	$\Psi_{CE} = (m+1)\lambda_s - m\lambda - \varpi_s$	$a_{CE} = 62930.793 \pm 0.124$
Arc geometrical radius		$a = 62932.330 \pm 0.030$

[a] From the mean motions of Table I and the method of Appendix A

here the secular perturbation forced by the satellite, as described out by Horanyi and Porco (1993). This effect shifts *all* the resonance radii by ~0.2 km, but it does not change the dynamical structure of the problem.

The orbital eccentricity of Galatea is compatible with zero, $e_s = 1.20\ (\pm 1.49) \times 10^{-4}$ (Owen *et al.* 1991, see Table I). Its orbital inclination, in the meantime, is nonzero: $I_s = 0.0544° \pm 0.0132°$ (*Ibid.*). We will thus take from now on $e_s = 0$, so that no term containing Ψ_{CE} will appear anymore. This simplifies the equations of motion, preserving however the essential coupling between the vertical and the horizontal motions of the particle.

In the case of Adams ring and Galatea, we have $m = -43$. The geometrical radii $a_{CI}, a_{LE}, a_{LI}, a_{CE}$ of the corresponding resonances are given in Table II. Note the close packing of the four resonances. There is another set of four resonances, corresponding to $m = -44$, located at 22.7 km inside the arcs radius, while the resonances corresponding to $m = -42$ lie 23.8 km outside it (Fig. 1). The two possible geometrical radii of the arcs are also marked with dots for comparison.

Near a mean motion resonance, the average motion of the particle is described by six scalar quantities

$$\begin{aligned} \chi &\equiv \frac{3}{2} m \frac{\Delta a}{a_{CI}} \\ \Psi_{CI} & \\ h &\equiv e \cdot \cos(\Psi_{LE}) \\ k &\equiv e \cdot \sin(\Psi_{LE}) \\ u &\equiv I \cdot \cos(\Psi_{LI}/2) \\ v &\equiv I \cdot \sin(\Psi_{LI}/2), \end{aligned} \tag{1}$$

where $\Delta a \equiv a - a_{CI}$. Physically, χ is the nondimensional distance of the particle guiding center to the corotation radius a_{CI}. The quantity χ, together with Ψ_{CI}, describes the motion of the particle *guiding center* near a corotation site.

The vector (h, k) will be referred to as the resonant eccentricity vector of the particle. Its position angle Ψ_{LE} is directly linked to the orbital phase of the particle at the conjunction with the satellite, i.e., also to the orientation of the particle scalloped trajectory as observed from the satellite (see Porco *et al.* 1995, and Fig. 14).

Similarly, (u, v) represents the resonant inclination vector of the particle. Its argument $\Psi_{CI}/2$ is linked to the orientation of the vertical arches followed by the particle above and below the planet equatorial plane, as observed from the satellite.

Finally, it will be useful to define a resonant inclination vector (u_s, v_s) for the satellite, as well as the *mutual* inclination vector (U, V) of the particle with respect to the satellite:

$$\begin{aligned} u_s &\equiv I_s \cdot \cos(\Psi_{CI}/2) \\ v_s &\equiv I_s \cdot \sin(\Psi_{CI}/2) \\ U &\equiv u - u_s \\ V &\equiv v - v_s. \end{aligned} \tag{2}$$

The mutual inclination is then $I_m = \sqrt{U^2 + V^2}$. The

TABLE III
Nondimensional Resonant Forcing Terms

ϵ_e	7.25×10^{-7}
ϵ_i	3.30×10^{-6}
j_p	-1.69×10^{-3}
j_n	-4.64×10^{-5}

method to calculate the rates of change of χ, Ψ_{CI}, h, k, u, and v forced by the three resonances (CIR, LER, and LIR) is outlined in Appendix A. These rates are

$$\begin{aligned}
\frac{d\chi}{d\tau} &= +3m^2[4\varepsilon_i(u-u_s)(v-v_s)+\varepsilon_e k] \\
\frac{d\Psi_{CI}}{d\tau} &= +2\chi \\
\frac{dh}{d\tau} &= -(\chi+j_p)k \\
\frac{dk}{d\tau} &= +(\chi+j_p)h-\varepsilon_e \\
\frac{du}{d\tau} &= -(\chi+j_n)v-2\varepsilon_i(v-v_s) \\
\frac{dv}{d\tau} &= +(\chi+j_n)u-2\varepsilon_i(u-u_s),
\end{aligned} \tag{3}$$

where we have defined, for sake of simplicity,

$$\begin{aligned}
\tau &\equiv nt \\
j_p &\equiv \frac{\dot\Omega_s-\dot{\bar\omega}}{n} \\
j_n &\equiv \frac{\dot\Omega_s-\dot\Omega}{n} \\
\varepsilon_e &\equiv -\alpha A\frac{M_s}{M_N} \\
\varepsilon_i &\equiv +\alpha V\frac{M_s}{M_N},
\end{aligned} \tag{4}$$

where $\dot\Omega_s$, $\dot\Omega$, and $\dot{\bar\omega}$ are the nodal and apsidal precession rates caused by the planet's oblateness. The numerical coefficients A and V are defined in Appendix A, and $\alpha = a/a_s$. The numerical values of j_p, j_n, ε_e and ε_i corresponding to $m = -43$ are given in Table III. The system (3) admits the following integral of motion

$$\begin{aligned}
C = \frac{\chi^2}{6m^2}+\varepsilon_i[(u_s-u)^2-(v_s-v)^2] \\
-\frac{j_p}{2}[(h-h_0)^2+k^2]-j_n\frac{I^2}{2},
\end{aligned} \tag{5}$$

where $h_0 \equiv \varepsilon_e/j_p$ is the eccentricity forced by the LER at the center of the arc (see Eq. (11)).

The numerical values of j_p, j_n, ε_e, and ε_i are given in Table III, for the specific case of the satellite Galatea and Adams ring. The quantity j_p is the satellite *nodal* precession rate *relative* to the particle *apsidal* precession rate, normalized to the mean motion n of the particle. The quantity j_n represents the *differential* nodal precession rate of the satellite and the particle. Because both nodes precess in the same (retrograde) direction, j_n is much smaller than j_p. We will see the importance of this result later.

Finally, the quantities ε_e and ε_i are both proportional to the mass of the satellite. Their numerical values represent the efficiency of the satellite to force the eccentric and inclined motions on the particle, respectively, near the corresponding resonances. Considering the mass estimated for Galatea ($M_s/M_N \sim 2.1 \times 10^{-8}$, see Porco 1991, and Table I), one gets the values of ε_e and ε_i given in Table III.

The system (3) can be split into three subsystems of two equations each, describing respectively the CIR (variation of χ and Ψ_{CI}), the LER (variations of h and k), and the LIR (variations of u and v). The mixing of the variables in this system indicates the coupling between the resonances. Note the nonlinearity of the system.

The small, but nonvanishing value of j_p causes the splitting of the LER and CIR radii (about 1.65 km, see Table II and Fig. 1), and the smaller value of j_n causes the splitting of the CIR and LIR (about 0.045 km). The smallness of j_p and j_n is responsible for the strong coupling between the resonances.

4. MAIN FREQUENCIES OF THE SYSTEM

4.1. Corotation Inclined Resonance

Neglecting for the moment the effect of the Lindblad resonances on the CIR, the system (3) reduces to the pendulum equation

$$\frac{d^2\Psi_{CI}}{d\tau^2} = 12m^2\varepsilon_i I_s^2\sin(\Psi_{CI}), \tag{6}$$

with the integral of motion $C = \chi^2/(6m^2) + \varepsilon_i I_s^2\cos(\Psi_{CI})$. This yields the total width of the libration zone where the particle guiding center can be trapped (we will call such zone a *corotation site*):

$$W_{CI} = a_{CI}I_s\sqrt{\frac{16}{3}\varepsilon_i}, \tag{7}$$

and the libration period near the center of the corotation site ($\Psi_{CI} = 180°$, $\chi = 0$):

$$T_{CI} = \frac{4}{3m}\frac{a_{CI}}{W_{CI}}T, \tag{8}$$

where $T = 2\pi/n$ is the orbital period of the particle.

The numerical values given in Tables I and II yield

$$W_{\rm CI} \sim 8.9 I_{\rm s}^{\circ} \text{ km}$$
$$T_{\rm CI} \sim \frac{0.26}{I_{\rm s}^{\circ}} \text{ years}, \tag{9}$$

where $I_{\rm s}^{\circ}$ is the satellite orbital inclination expressed in degrees. For the nominal value of $I_{\rm s} = 0.0544°$, we get $W_{\rm CI} = 0.48$ km and $T_{\rm CI} = 4.8$ years. This typical libration period can be noted in Fig. 6b, for instance.

It is important to note that the libration period is given here for the *center* of the corotation site. As one moves toward the separatrix of the site, $T_{\rm CI}$ actually tends to infinity. Thus, many of the arc particles observed in Adams ring have expected libration periods much longer than the value ~5 years quoted above.

4.2. Lindblad Eccentric Resonance

We now consider the LER acting alone, i.e., with only planar motions ($I = I_{\rm s} = 0$) and with a circular orbit for the satellite. The system (3) then becomes

$$\begin{aligned} \frac{dh}{d\tau} &= -(\chi + j_{\rm p})k \\ \frac{dk}{d\tau} &= +(\chi + j_{\rm p})h - \varepsilon_{\rm e} \\ \frac{d\chi}{d\tau} &= 3m^2\varepsilon_{\rm e}k \\ \frac{d\Psi_{\rm CI}}{d\tau} &= 2\chi. \end{aligned} \tag{10}$$

This two degree of freedom system admits two integrals of motion, $J \equiv e^2 + 2(\chi + j_{\rm p})/3m^2$ and $K \equiv e^4 - 2Je^2 + (8\varepsilon_{\rm e}/3m^2)h$, and is thus integrable. The quantity J is the averaged value of the Jacobi constant.

The fixed points of the System 10 must verify $\dot{h} = 0$ (i.e., $k = 0$) and $\dot{k} = 0$, which yields the forced eccentricity

$$e_{\rm forced} = |h| = \frac{\varepsilon_{\rm e}}{|\chi + j_{\rm p}|}. \tag{11}$$

Porco (1991) uses this relation in the middle of the arcs ($\chi = 0$) and the *observed* forced eccentricity of the arcs, 4.7×10^{-4}, to derive $\varepsilon_{\rm e}$, and thus the nominal value of $M_{\rm s}/M_{\rm N} = 2.07 \times 10^{-8}$ that we use in this paper.

The linearization of the system (10) near the stable fixed points shows that the oscillation of (h, k) around these points has a frequency $n_{\rm forced} = 3m^2\sqrt{(J - h^2)(J - 3h^2)}n/2$. Thus,

$$n_{\rm forced} = n|\chi + j_{\rm p}|\sqrt{1 - 3m^2\frac{\varepsilon_{\rm e}^2}{(\chi + j_{\rm p})^3}}. \tag{12}$$

At the center of the corotation site ($\chi = 0$), we obtain

$$e_{\rm forced} \sim 2.0 \times 10^4 \frac{M_{\rm s}}{M_{\rm N}}$$
$$T_{\rm forced} \sim 0.57 \text{ years}. \tag{13}$$

Note again that $T_{\rm forced}$ may be much longer if (h, k) follows a trajectory close to a separatrix.

4.3. Modulation of the Mutual Inclination

The width of a corotation site at a given moment actually depends on the *mutual* inclination $I_{\rm m} = \sqrt{U^2 + V^2}$ of the particle and the satellite at that moment. Thus, $I_{\rm m}$ should appear in place of $I_{\rm s}$ in Eq. (7), in the 3-D case. Now, because of the differential nodal precession rate of the particle and the satellite, $I_{\rm m}$ is slowly modulated with time. More precisely, the last two equations in (3) yield

$$\frac{d}{d\tau}(I_{\rm m}^2) = -8\varepsilon_{\rm i}UV + 2j_{\rm n}I_{\rm s}I\sin(\Omega_{\rm s} - \Omega). \tag{14}$$

Since we have $UV = \mathcal{O}(I_{\rm s}I)$, $\varepsilon_{\rm i} \sim 3.3 \times 10^{-6}$, and $j_{\rm n} \sim -4.6 \times 10^{-5}$, the dominating term on the right-hand side of the equation above is that containing $\sin(\Omega_{\rm s} - \Omega)$. The latter is in turn modulated by the differential nodal precession rate between the satellite and the particle, with the period $2\pi/(nj_{\rm n})$. In other words, the forcing term due to the satellite ($-8\varepsilon_{\rm i}UV$) is too small, by a small margin, to control the variations of the mutual inclination (U, V). The modulation period of $I_{\rm m}$ is thus

$$T_{\rm modul} = \frac{T}{|j_{\rm n}|} \sim 26.7 \text{ years}. \tag{15}$$

In conclusion, the Lindblad eccentric resonance forces a period of ~7 months or more on the eccentricity of the particle. The corotation inclined resonance forces libration motions for the guiding centers of the particles of ~5 years or more, for $I_{\rm s} = 0.0544°$. Finally, the very small differential nodal precession of the particle and the satellite creates a slow modulation (~27 years) of the mutual inclination of the satellite and the particle.

From a more physical point of view, the resonant motion of a particle in Adams ring is akin to that of a pendulum with a period of order 5 years, and whose length is slowly varied over a period of order 27 years, while it receives (or loses) energy over a typical period of 7 months.

5. COUPLING BETWEEN THE RESONANCES

The original descriptions of corotation trapping assume that the motion driven by the CIR potential entirely decouples from the LER potential, and also that the vertical motion entirely decouples from the horizontal motion. Because the three resonances considered here are so close

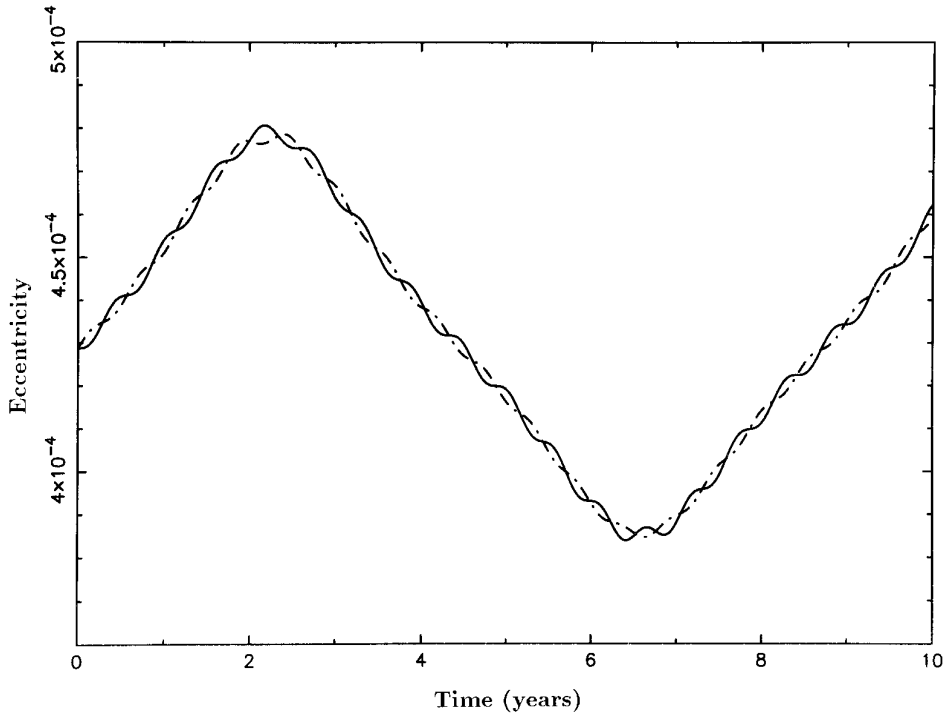

FIG. 2. Actual evolution of the particle orbital eccentricity with time (solid line) compared with the eccentricity expected from an adiabatic invariant argument (dot–dashed line), see Section 5.1 for discussion.

together, we will see that the actual motion of the particle can be quite complicated.

5.1. Adiabatic Invariance Associated with the Eccentricity

Before embarking in a more complete analysis, we note that there is a situation where the system (3) is relatively simple to solve, at least approximately. The stable equilibrium point of this system (obtained when all the time derivatives are zero) must satisfy $\chi = 0$, $\Psi_{CI} = 180°$, $h = h_0 = \varepsilon_e/j_p$, and $k = 0$. In other words, the particle must be right at the center of the corotation site and have the equilibrium eccentricity $|\varepsilon_e/j_p|$.

As we get away from this equilibrium situation, the particle guiding center starts a slow ($\sim$5 years) libration motion in the corotation site, while the eccentricity vector oscillates on a quite shorter time scale ($\sim$7 months or more). We are thus ensured in this case of the adiabatic invariance of the area enclosed in the trajectory of (h, k).

In particular, suppose we start with a particle at $\chi \neq 0$, with the forced eccentricity $\varepsilon_e/(\chi + j_p)$ corresponding to that radius. Then the eccentricity must keep the value $\varepsilon_e/(\chi + j_p)$ as the particle slowly drifts back and forth across the corotation site, exploring various values of χ. This is because the forced value corresponds to a zero area enclosed in the (h, k) trajectory, and also because this area must keep its zero value by the adiabatic invariance. This is illustrated in Fig. 2, where the actual eccentricity (solid line) is plotted together with the "adiabatic" value, $\varepsilon_e/(\chi + j_p)$. One can note the excellent agreement between these two values at any moment.

As a consequence, and for such particles, there exists an eccentricity gradient between the inner and outer edges of the corotation site. In the extreme case where a particle explores the full width of a corotation site, its semi-major axis varies by $\pm W_{CI}/2 = \pm 0.24$ km, corresponding to $\chi = \pm 2.3 \times 10^{-4}$, while $j_p \sim -1.7 \times 10^{-3}$. This creates an eccentricity gradient $a\Delta e/a = 3m\varepsilon_e/2j_p^2 \sim -16.3$. The physical width W of the arcs is then dominated by this gradient and can reach a value of $\sim$7 km across the full width of the corotation site. This point will be discussed again later, especially when collisions are considered.

5.2. The Semi-planar Problem: Regular and Chaotic Motion

We may have a good insight of the dynamics of a test particle by first considering the case where the satellite has an inclined orbit, thus creating a corotation site, but where the particle is forced (artificially) to move in the equatorial plane of the planet, i.e., with $u = v = 0$. We loosely refer to this case as the "semi-planar" problem. It allows us to better understand the 3-D structure of the problem, but it remains simple enough for the classical surface of section method to be used. The system (3) then turns into

$$\begin{aligned}\frac{d\chi}{d\tau} &= +3m^2[2\varepsilon_i I_s^2 \sin(\Psi_{CI}) + \varepsilon_e k]\\ \frac{d\Psi_{CI}}{d\tau} &= +2\chi\\ \frac{dh}{d\tau} &= -(\chi + j_p)k\\ \frac{dk}{d\tau} &= +(\chi + j_p)h - \varepsilon_e.\end{aligned} \tag{16}$$

The integral of motion of this system is obtained from Eq. (5), where $u = v = I = 0$:

$$C_0 = \frac{\chi^2}{6m^2} + \varepsilon_i I_s^2 \cos(\Psi_{CI}) - \frac{j_p}{2}[(h - h_0)^2 + k^2]. \tag{17}$$

The subscript 0 in C_0 reminds us that we force here the particle to have a zero inclination.

The system (16) admits a stable fixed point at $\chi = 0$, $\Psi_{CI} = 180°$ (center of the corotation site), with the forced eccentricity $h \equiv h_0 = \varepsilon_e/j_p$, $k = 0$. We would like to know what happens as we get farther away from this fixed point.

The system (16) describes a two-degree of freedom dynamical system (essentially a pendulum receiving or yielding energy from or to the Lindblad resonance) with an integral of motion, C_0. Consequently, surfaces of section can be made to disentangle the complex motion of the particle.

Namely, we fix a value for C_0, and we plot the value of $(\Psi_{CI}, \Delta a = 2\chi a_{CI}/3m)$ every time the trajectory goes through the surface $k = 0$. Actually, there are two possible trajectories going through the point $(\Psi_{CI}, \Delta a)$, corresponding to the two roots h_1 and h_2 of the equation in h, $C_0 = \chi^2/6m^2 + \varepsilon_i I_s^2 \cos(\Psi_{CI}) - j_p/2(h - h_0)^2$. Choosing always the larger root then ensures the uniqueness of the orbit. We do not use the criterion $\dot{k} > 0$ (or $\dot{k} < 0$), because two different trajectories going through the point $(\Psi_{CI}, \Delta a)$ may have both $\dot{k} > 0$ (or both $\dot{k} < 0$).

Physically, the surface of section shows the position of the particle guiding center every time the conjunction with the satellite occurs at the periapse or the apoapse of the particle.

Because $j_p < 0$, Eq. (17) shows that we always have $C_0 \geq -\varepsilon_i I_s^2$. Also, the existence of two real roots h_1 and h_2 requires $\chi^2/6m^2 + \varepsilon_i I_s^2 \cos(\Psi_{CI}) \leq C_0$. This in turn defines an accessible region for the guiding center in the (Ψ_{CI}, χ) plane, once C_0 has been given. In particular, for

$$-\varepsilon_i I_s^2 \leq C_0 \leq \varepsilon_i I_s^2 \tag{18}$$

the surface of section is confined in a finite interval of Ψ_{CI} inside 0°–360°, and also in a finite interval of Δa. Consequently, the particle cannot escape the corotation site in this case. An example of such a surface of section is shown in Fig. 3a. In contrast, if the value of C_0 is increased above $\varepsilon_i I_s^2$, some particles have access to the circulating region, see Fig. 3b.

We see that the surfaces of section reproduce the general structure of the pendulum phase portrait. Note, however, the distortion induced by the coupling between the CIR and LER. For instance, the libration center in Fig. 3b is located at ~ -0.8 km from the CIR radius. Remember also that the *actual* motion of the particle guiding center is quite more complicated than the trajectories shown in Fig. 3b.

An example is given in Fig. 4, where $(\Psi_{CI}, \Delta a)$ is plotted not only when $k = 0$, but also at every time step (18.25 days in this particular integration). The guiding center of the particle is initially placed at -1.05 km from the CIR radius, and at $\Psi_{CI} = 180°$. The eccentricity vector of the particle is then $h = -6.54 \times 10^{-5}$, $k = 0$. The total integration time represents 200 years. Note that the guiding center of the particle actually explores a symmetrical region around $\Delta a = 0$, due to the variation in free eccentricity of the orbit with time. This radial forcing has the typical period of $\sim$7 months or more calculated in Eq. (13). Superimposed to that relatively fast period is the slower $\sim$5 years libration motion estimated in Eq. (8).

Even though the corotation site in the surface of section has a width of $\sim$0.75 km (Fig. 3b), the guiding center is actually able to explore a much larger region of width $\sim$2.15 km. It is even able to reach or go beyond the unstable saddle points at $\Psi_{CI} = 0°$ or 360°, while remaining trapped in the corotation site. This may have important consequences for the material distribution in Neptune's arcs: particles can cross the separatrix between two arcs, but have nevertheless a stable motion in one of them.

As noted above, this effect is caused by the free eccentricity of the particle. In the present simulation, the particle does not suffer any collisions with other particles. In a real arc, however, collisions will randomize the free eccentricity and result in a motion even more complicated than in Fig. 4. The eventual stability of the particle motion in the corotation site is thus a more subtle matter than just having the semi-major axis of the particle at ± 0.24 km from the CIR radius (see Eq. (7)).

As C_0 is increased, a chaotic zone appears in the surface of section, see Fig. 5. The initial conditions for the particles having a chaotic motion are still quite plausible in the case of Neptune's arcs. For instance, the particle in the chaotic zone of Fig. 5a starts with an eccentricity $\sim 10^{-4}$, on the order of magnitude of the eccentricity of the arcs, $\sim 4.7 \times 10^{-4}$. Note also that the chaotic zone does not affect the stability of the corotation sites themselves, which stay in the regular part of the diagram. This is true in the semi-planar problem we are considering here, but not anymore in the full 3-D problem we will investigate now.

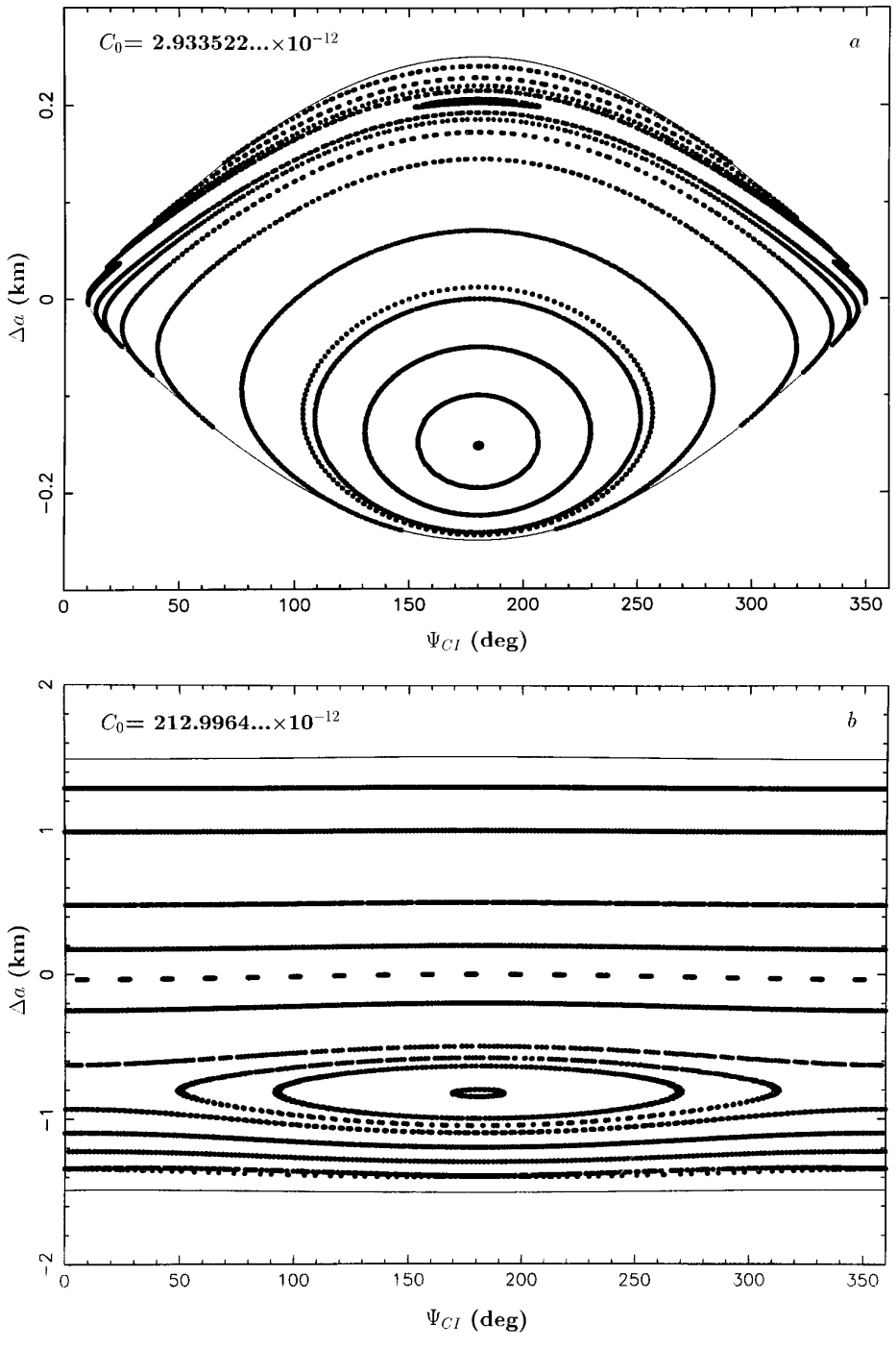

FIG. 3. (a) Surface of section showing the topology of the dynamical system described by the semi-planar system (16). The latter describes the average motion of a particle orbiting in the equatorial plane of the planet and perturbed by an inclined satellite. The positions of the particle guiding centers are plotted every time $k = 0$. The reference radius ($\Delta a = 0$) corresponds to the corotation inclined resonance (CIR) radius. The actual mean longitude of the particle inside the corotation site is $\lambda = \Psi_{CI}/2|m|$, with $m = -43$. In this example, the constant C_0 (Eq. (17)) is 2.933522 ... $\times 10^{-12}$, and all the particles remain trapped in the corotation site because $C_0 < \varepsilon_i I_s^2$ (Eq. (18)). Note, however, the distortion of the site due to the interaction with the LER, with respect to the classical pendulum phase portrait. (b) Another surface of section, with $C_0 = 212.996 ... \times 10^{-12}$. Some particles can now have libration motions. Note the change of the radial scale between (a) and (b).

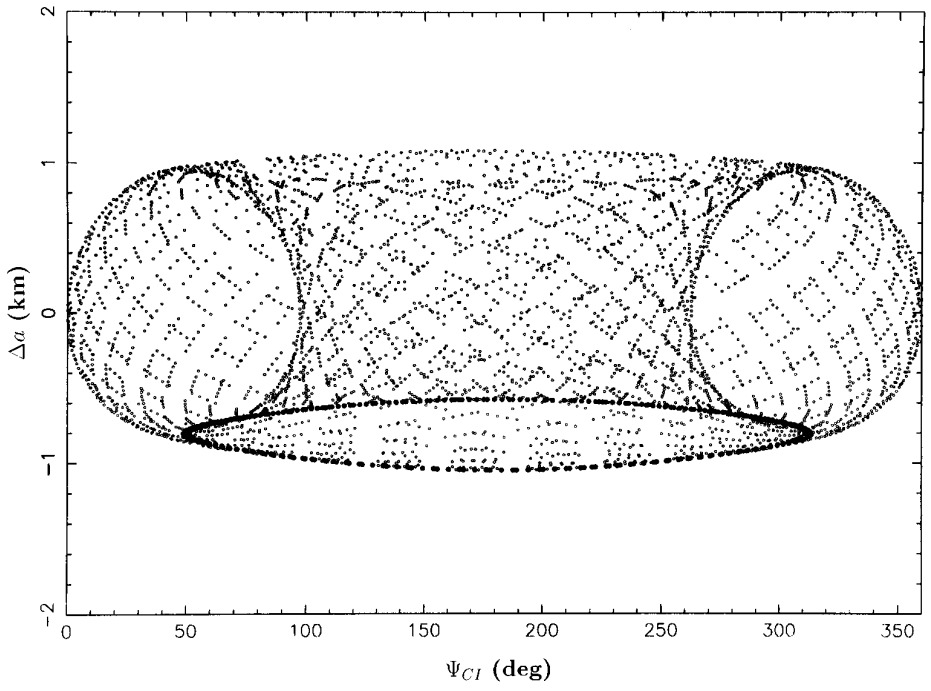

FIG. 4. Actual motion of the guiding center for one of the particles of Fig. 3b. The guiding center of the particle is plotted every 18.25 days, and the overall duration of the integration is 200 years. The larger dots at the bottom are those corresponding to one of the surfaces of section $k = 0$ already shown in Fig. 3b. Note that the particle semi-major axis actually explores a quite wider region than indicated by the surface of section itself. Note also that although $\Psi_{\rm CI}$ can go just beyond 0° or 360°, the particle is still stably trapped into the libration site. See the text for discussion.

5.3. The 3-D Case: Stochastic Migration from Site to Site

We now relax the constraint $u = v = 0$ (planar motion of the particle), and we integrate the full 3-D system (3). Figure 6a shows the position of the guiding center of a particle whenever $k = 0$, superimposed to the surface of section already shown in Fig. 3b. Note that each point $(\Psi_{\rm CI}, \Delta a)$ does *not* define uniquely an orbit anymore, since we have a new degree of freedom associated with the vertical motion of the particle. We see that the particle can now explore successively the libration and the circulation regions of the phase space.

This behavior is shown more readily in Fig. 6b, where the longitude λ of the particle is plotted in a frame rotating with the corotation potential, which revolves at the angular velocity $n_{\rm CI} = [(m + 1)n_{\rm s} - \dot{\Omega}_{\rm s}]/m$. The angle $\lambda_{\rm CI}$ thus denotes the quantity $n_{\rm CI}t$ in this diagram and some of the followings. We clearly see the wandering of the particle from one site to the other during the 1200 years of the integration. Episodes of captures, which may last up to $\sim$50 years, are irregularly interrupted by migrations from one site to the adjacent site. Also plotted for comparison is the (regular) libration of the particle in the semi-planar case.

This wandering is modulated by the $\sim$27 years oscillation of the mutual inclination $I_{\rm m}$ forced by the differential nodal precession rate of the particle and the satellite (Eq. (15)). This slow modulation modifies the width the actual corotation site felt by the particle, as explained in Section 4.3 (see also Fig. 6a). Of course, we can choose particles which are sufficiently inside the corotation site for this migration to be inhibited, or sufficiently outside the site for any capture to be impossible. The important point is that even the averaged problem exhibits an inherently chaotic nature. This allows the particles to diffuse from arc to arc even in the absence of any dissipation.

As expected, this character will be confirmed when we integrate the motion of the particles with the mapping method, which takes into account the high-frequency terms of the satellite perturbations.

6. THE MAPPING METHOD

The general philosophy adopted now is to consider that the particle orbits close enough to the satellite so that the latter gives little instantaneous "kicks" to the particle at each conjunction. These kicks remain small if the particle does not orbit too close to the satellite, or more precisely, to its Hill radius $R_{\rm H} = a_{\rm s}H$, where the reduced Hill radius H is

$$H \equiv \left(\frac{M_{\rm s}}{3M_{\rm N}}\right)^{1/3}. \tag{19}$$

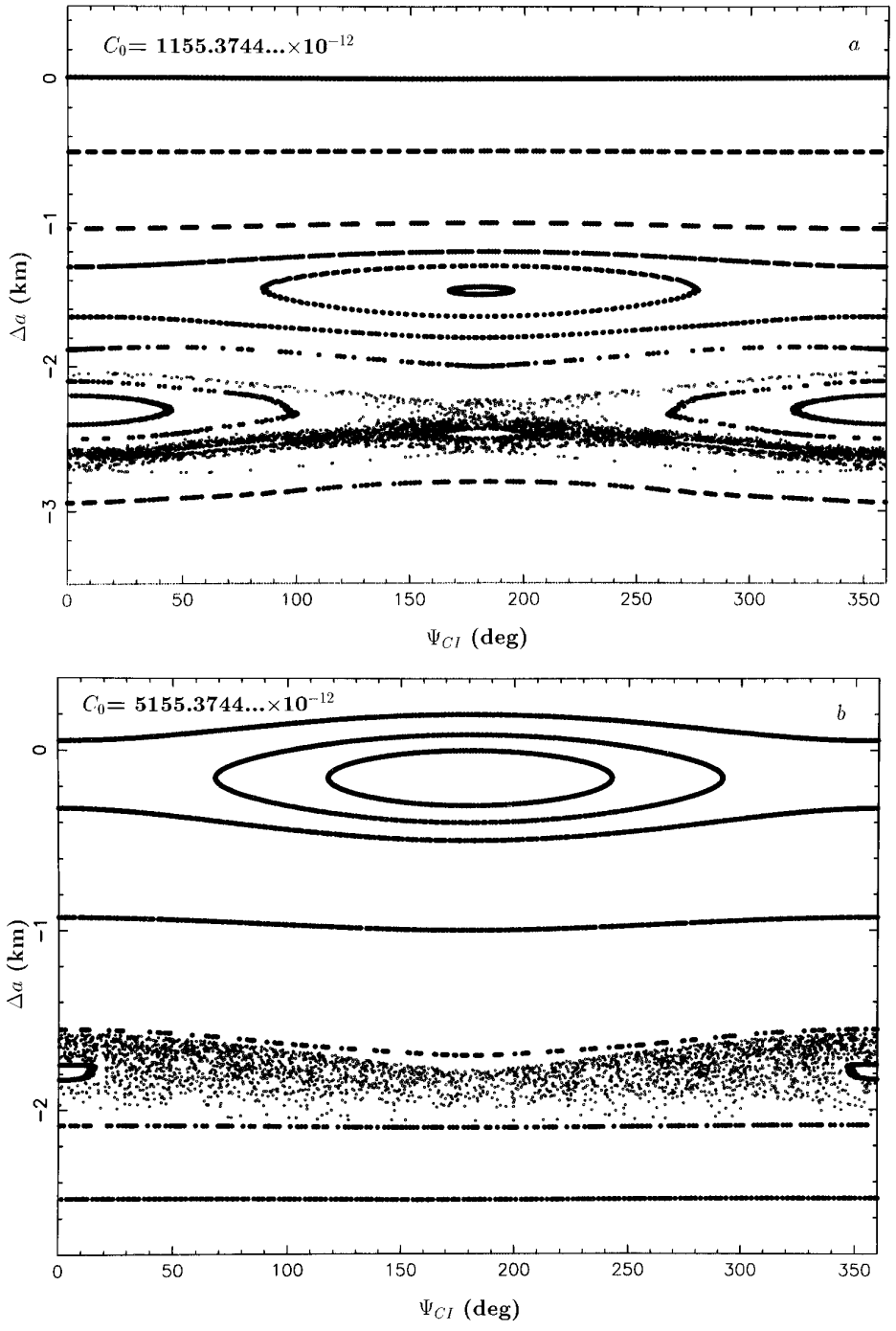

FIG. 5. (a) Same as described in the legend to Fig. 3, but with C_0 = 1155.3744 ... × 10^{-12}. Note the appearance of a chaotic zone just below the corotation site. Note also that the corotation site itself is not affected by chaoticity. (b) Same as above, but with C_0 = 5155.3744 ... × 10^{-12}. The islands near 0° or 360°, and $\Delta a = -2$ km, do *not* correspond to stable libration motions, but to circulation of Ψ_{CI}.

The kicks cause small discontinuities in the orbital elements of the particle and are described by a 3-D mapping.

The advantage of the mapping in this context is that it is tremendously fast compared to classical numerical integrators (see, for instance, the discussion by Kolvoord and Burns, 1992). Some care must be taken, however, in the derivation of the mapping, as explained in Appendix B. Also, the mapping is very general and can readily make use of any small mass for the satellite, at any distance

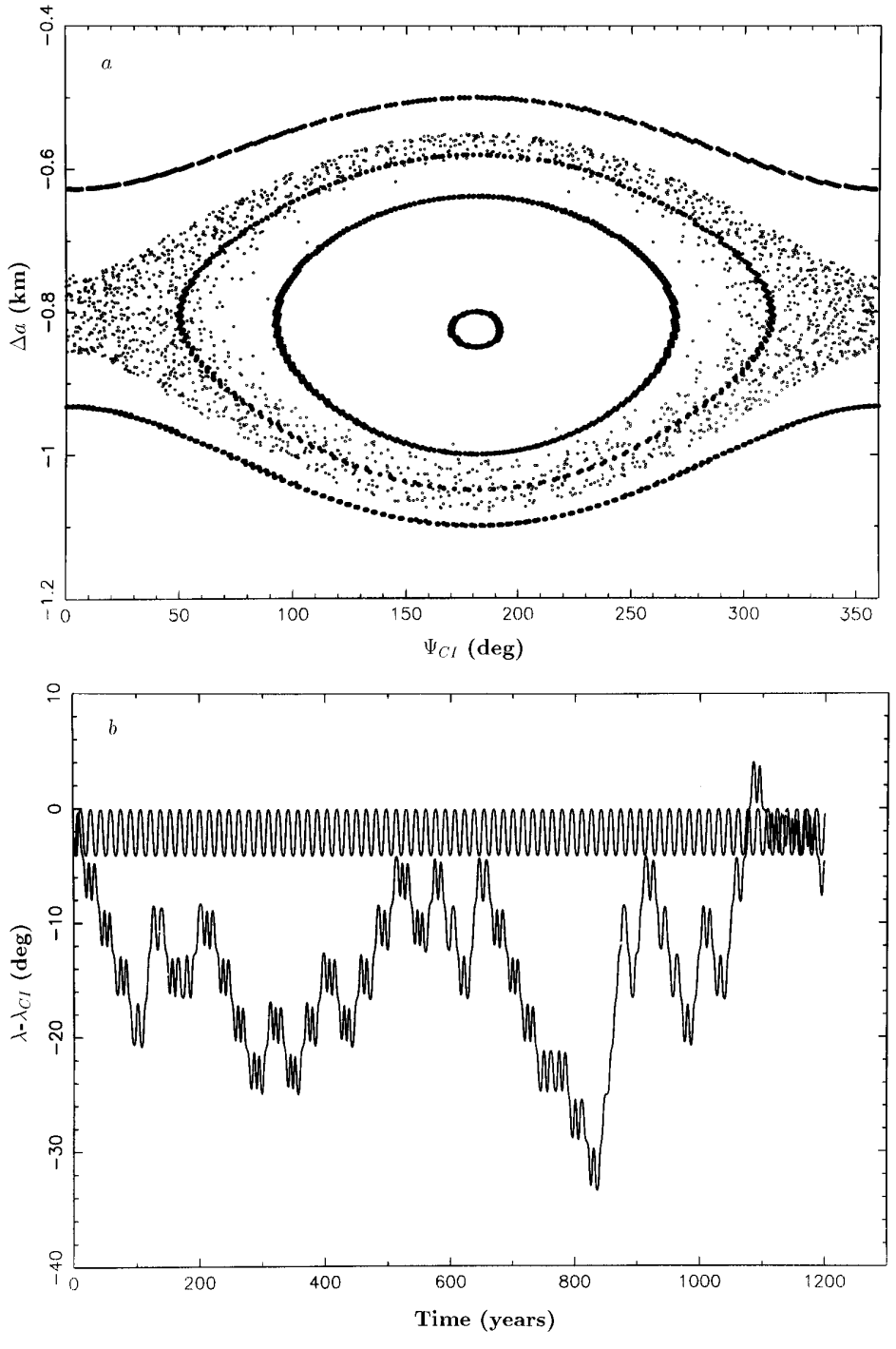

FIG. 6. (a) The regular curves are a part of the surface of section of Fig. 3b (semi-planar problem), while the scattered points are a surface of section where the particle is allowed to have a 3-D motion. This new degree of freedom allows the particle to alternate chaotically between libration and circulation motions. (b) The longitude of the particle shown in (a) is plotted vs time, in a frame revolving with the corotation potential. This plot is obtained by integrating the averaged equations of system (3). Note the sudden jumps from one corotation site to the other. For comparison, we also plot the regular motion of a particle starting with the same initial conditions, but that we force to have a 2-D motion (semi-planar problem, integration of system (16)).

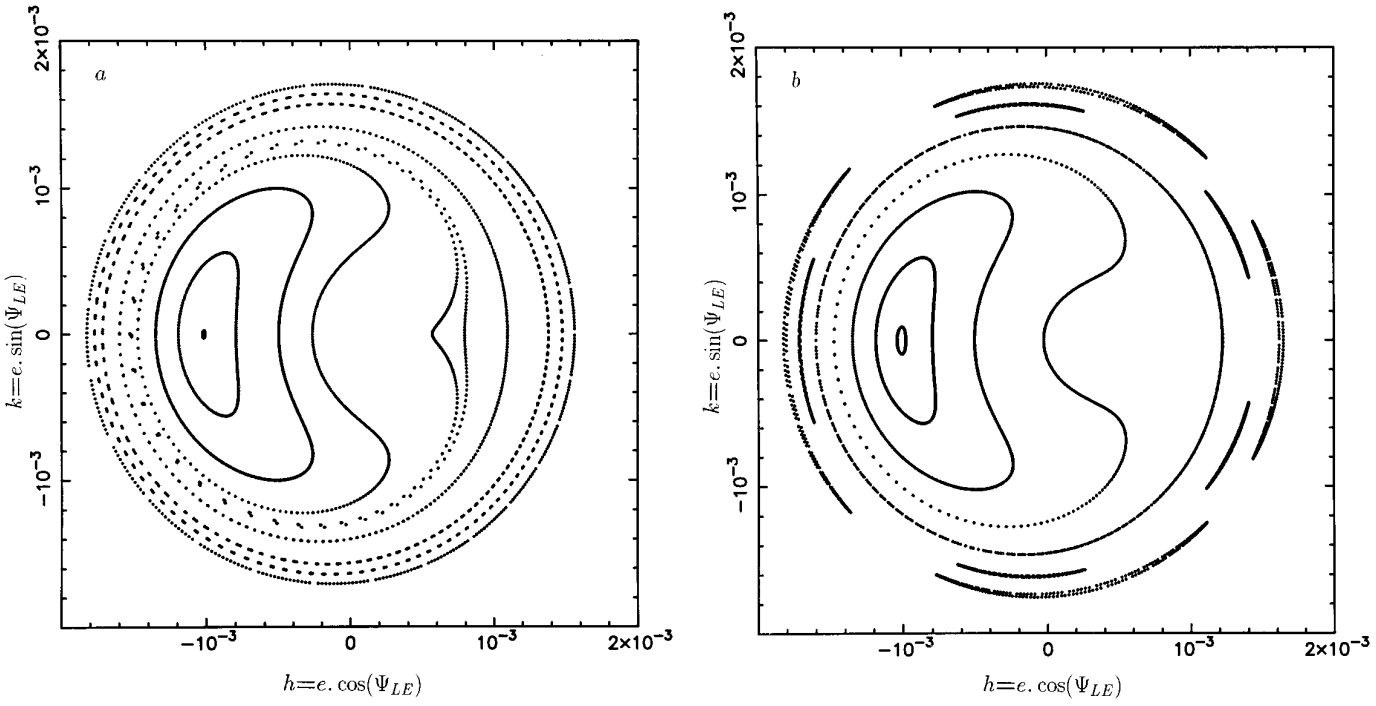

FIG. 7. Test of the validity of the mapping integration. We have chosen to compare the phase portrait of the LER, assuming a 2-D motion for both the satellite and the particle, and a circular orbit for the satellite. (a) Result using the averaged equations (10), with a fixed value of J and various values of K. (b) Result using the mapping. Each trajectory shown in (a) has been reintegrated by the mapping, using the same initial conditions in each case. See Section 6 for discussion.

from the ringlet (within the constraints listed below). This contrasts from Showalter and Burns' (1982) 2-D approach, for which a specific tabulation of the perturbation integrals is necessary for each new case of interest.

We derive the mapping expression from the 3-D Hill equations of motion. In this context, the particle motion is described by a set of six epicyclic elements, which are constant when no perturbation is applied, and which vary suddenly at each conjunction with the satellite. These epicyclic elements are the equivalent of the osculating orbital elements in the perturbed Keplerian motion. They are used here because they are better adapted to the particular geometry of our problem. The mapping thus provides the discontinuous variations of these epicyclic elements during a conjunction with the satellite.

The practical implementation of the mapping is described in Appendix B. It is derived under the following assumptions:

- The mass of the satellite is much smaller than the mass of the planet: $M_s \ll M_N$.
- The ring particles are massless.
- The orbital separation of the particle and the satellite is small compared to the orbital radius of the satellite or the particle: $|a - a_s| \ll a_s, a$.
- The orbital separation $|a - a_s|$ is large compared to the Hill radius $R_H = a_s H$ of the satellite.
- The orbital separation $|a - a_s|$ oscillates around a constant average value (i.e., there is no long-term *drift* of the particle semi-major axis).
- The radial and vertical displacements of the satellite and the particle are small compared to the orbital separation: $a_s e_s$, $a_s i_s$, ae, $ai \ll |a - a_s|$.

These conditions hold for the Adams ring and Galatea, since $M_s = 2.12 \times 10^{21}$ g, $|a - a_s| = 980$ km, $R_H = 119$ km, i.e., $M_s/M_N \sim 2.07 \times 10^{-8} \ll 1$, $|a - a_s|/a \sim 1.6 \times 10^{-2} \ll 1$, $R_H/|a - a_s| \sim 0.12$, and the radial and vertical excursions of the arcs (~30 km, Porco 1991) are small compared to $|a - a_s| \sim 980$ km.

The mapping must have several qualities: (i) give an accurate description of the effect of an *individual* conjunction with the satellite, (ii) conserve the Jacobi constant (Eq. (B14)), (iii) conserve the areas in the planes of the eccentricity and inclination vectors (symplecticity), and (iv) reproduce on the long term the phase portraits of the resonances. The methods used to fulfill these requirements are discussed in Appendix B.

We test the mapping in the simplest case where both the particle and the satellite have zero orbital inclinations,

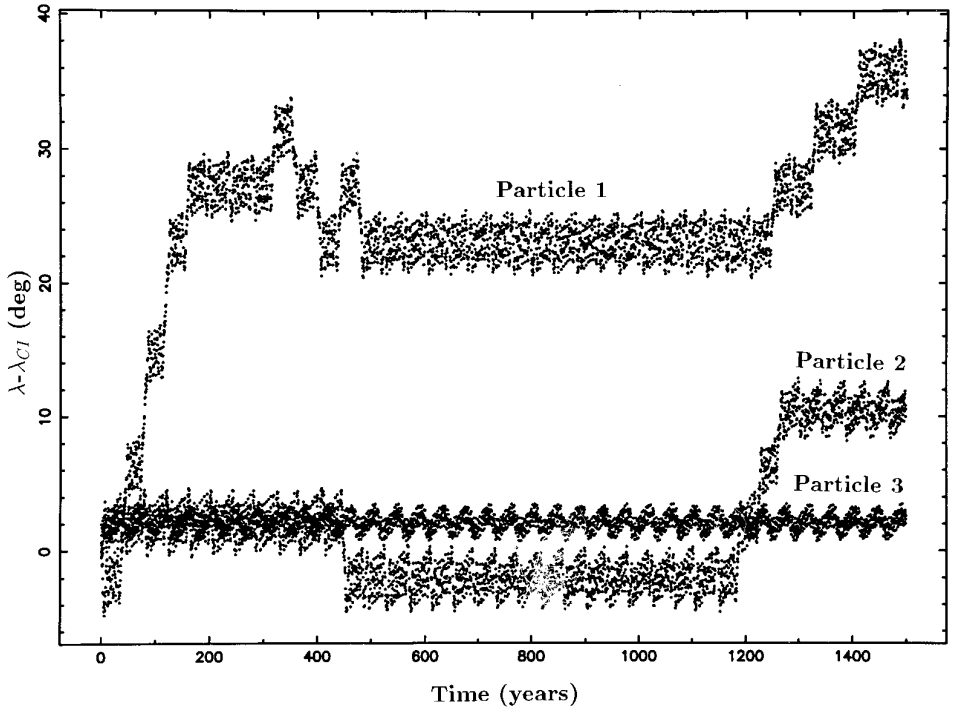

FIG. 8. The mean longitude of three test particles as a function of time. Their motions have been integrated by the mapping method, with no dissipation applied. The longitude is plotted in a frame revolving with the corotation sites. We used three slightly different initial positions for the particles, to show the transition between a stochastic migration from site to site (particle 1) to a stable libration inside the initial site (particle 3). Compare with the behavior observed in Fig. 6b. Note the smoothness of the curves in the latter diagram compared to those here, which was due to the averaging of the high-frequency terms.

and the satellite has a circular orbit. There is in this case only one resonance at work, namely the LER. The corresponding averaged problem has been described in Section 4.2, system (10), and the corresponding phase portrait is shown in Fig. 7a. Figure 7b shows the results of the mapping integration. More precisely, for each invariant curve shown in Fig. 7a, we have integrated in Fig. 7b the motion of the particle with the mapping, using the same initial conditions. One can note the excellent qualitative and quantitative agreements between the two methods at low eccentricity. Note, however, the "islands" which appear in the mapping integrations for eccentricities larger than $\sim 1.2 \times 10^{-3}$. They are due to higher order terms in the perturbing potential of the satellite and to the couplings with the nearby mean motion resonances corresponding to $m = -42$ and $m = -44$.

7. STOCHASTIC MIGRATION IN ADAMS RING: THE GRAVITATIONAL CASE

From now on, we use the mapping to integrate the motion of the particles. Thus, the high-frequency terms due to the conjunctions with the satellite will be accounted for. As we have already pointed out in the Introduction, it is important to note that the mapping is actually an integrator. Consequently, it takes into account both high-frequency terms and resonant terms of any order, whether they are overlapping or not.

In a first step, we consider only test particles perturbed by gravitational conservative forces from the satellite and from the planet's oblateness. This case is relevant to large particles inside the Adams ring, for which dissipative forces may be neglected.

7.1. Site to Site Migration: Effect of Initial Conditions

We consider the motion of three test particles with different initial conditions (Fig. 8). Particle 1 is placed near the separatrix between two adjacent sites, while particles 2 and 3 are located further inside. Figure 8 shows the mean longitude of each particle as a function of time, in a frame corotating with the arcs. While particle 3 remains trapped for 1500 years (more than 10^6 revolutions), particle 2 and especially particle 1 suffer a stochastic diffusion from one site to the other. This confirms the behavior found in

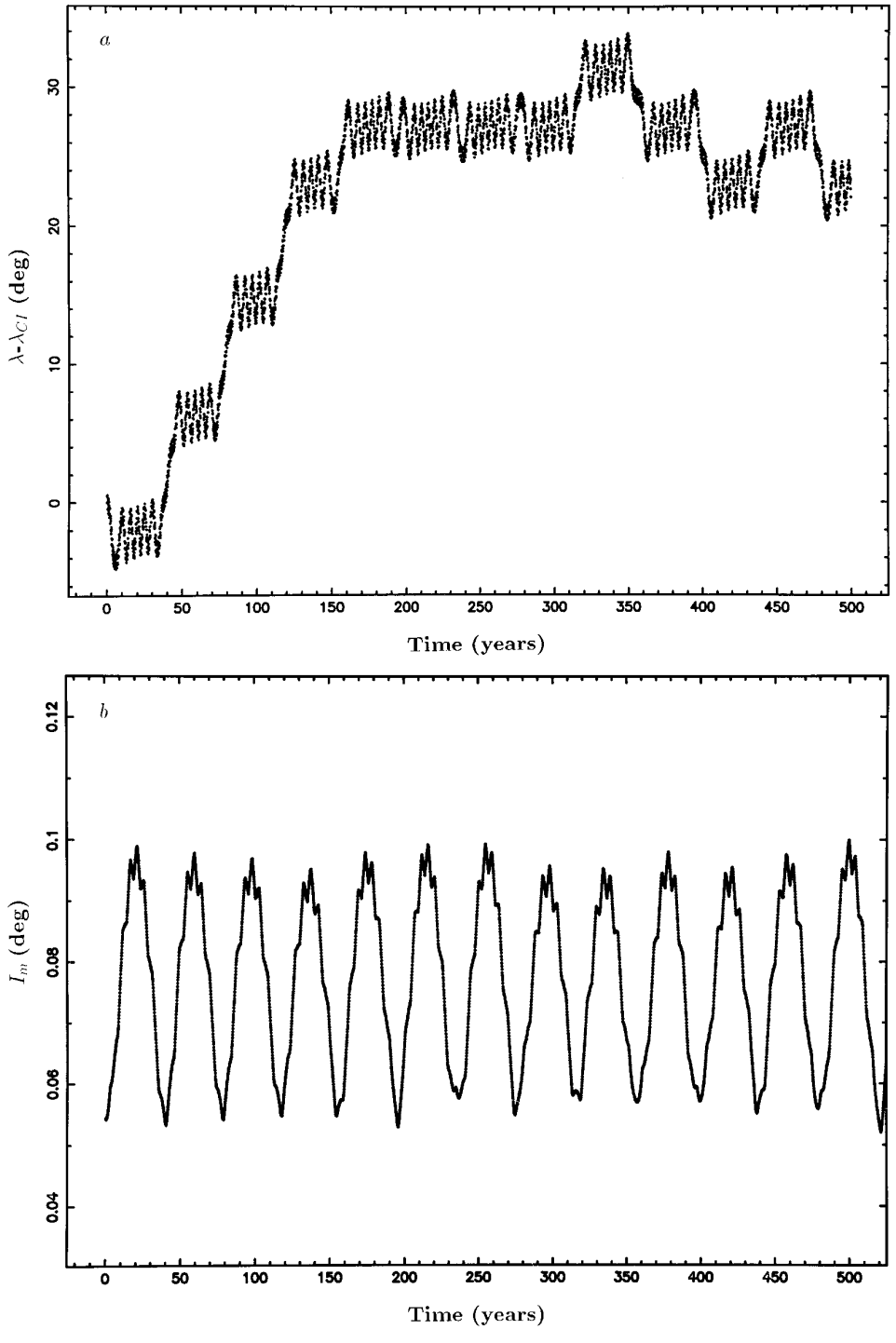

FIG. 9. (a) Close-up of the motion of particle 1 shown in Fig. 8 at small times. (b) The mutual inclination I_m of the particle and the perturbing satellite as a function of time. Note the clear correlation between the migration from site to site and the fact that I_m reaches a minimum value. See the discussion in Section 5.3.

Section 5.3, using the averaged equations, as illustrated in Fig. 6b.

Figure 9 shows the clear correlation between the migration phases of particle 1 from one site to the other, and the times when the mutual inclination I_m of the particle and the satellite is minimum. This is in agreement with the results shown in Fig. 6a: the migrations occur when the corotation site is narrowest, i.e., when I_m is smallest.

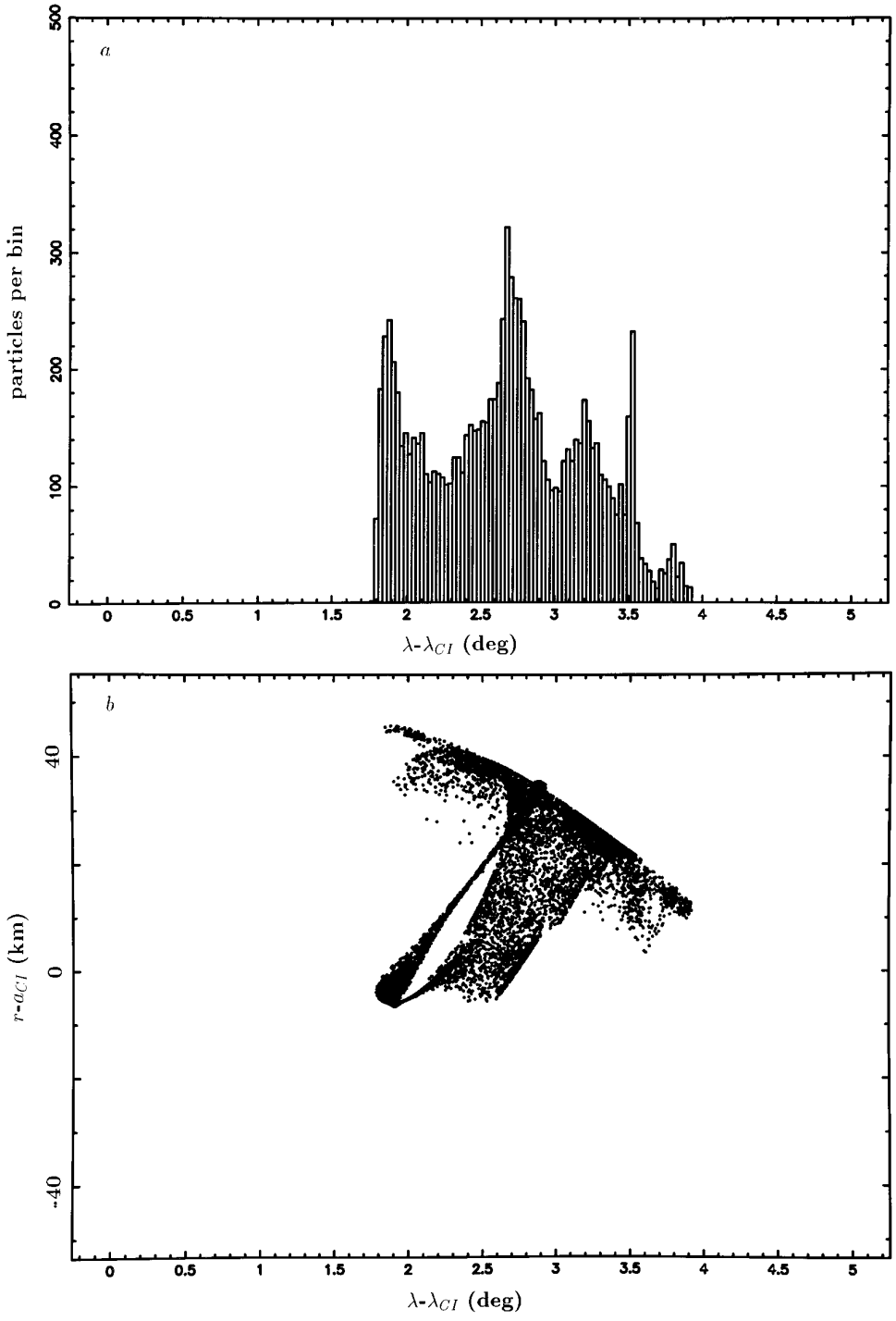

FIG. 10. Evolution of 10^4 test particles released at time $t = 0$ at the location of particle 3 of Fig. 8, but with a random 3-D velocity ranging from 0 to 1 cm sec^{-1}, simulating the effect of dust ejection from a parent body. (a) Azimuthal density distribution of the particles after $t = 500$ years. (b) Positions of the particles in a longitude-radius diagram at the same time. The radial distances are counted from the CIR radius.

7.2. Site to Site Migration: Particles Released at the Same Location

We now consider the effect of slightly different initial conditions on the evolution of a swarm of particles (no dissipation is applied yet). The aim pursued here is to see how a cloud of particles released from a parent body will diffuse in an arc, and eventually in the continuous part of the ring. To do so, we consider 10^4 particles launched from the same

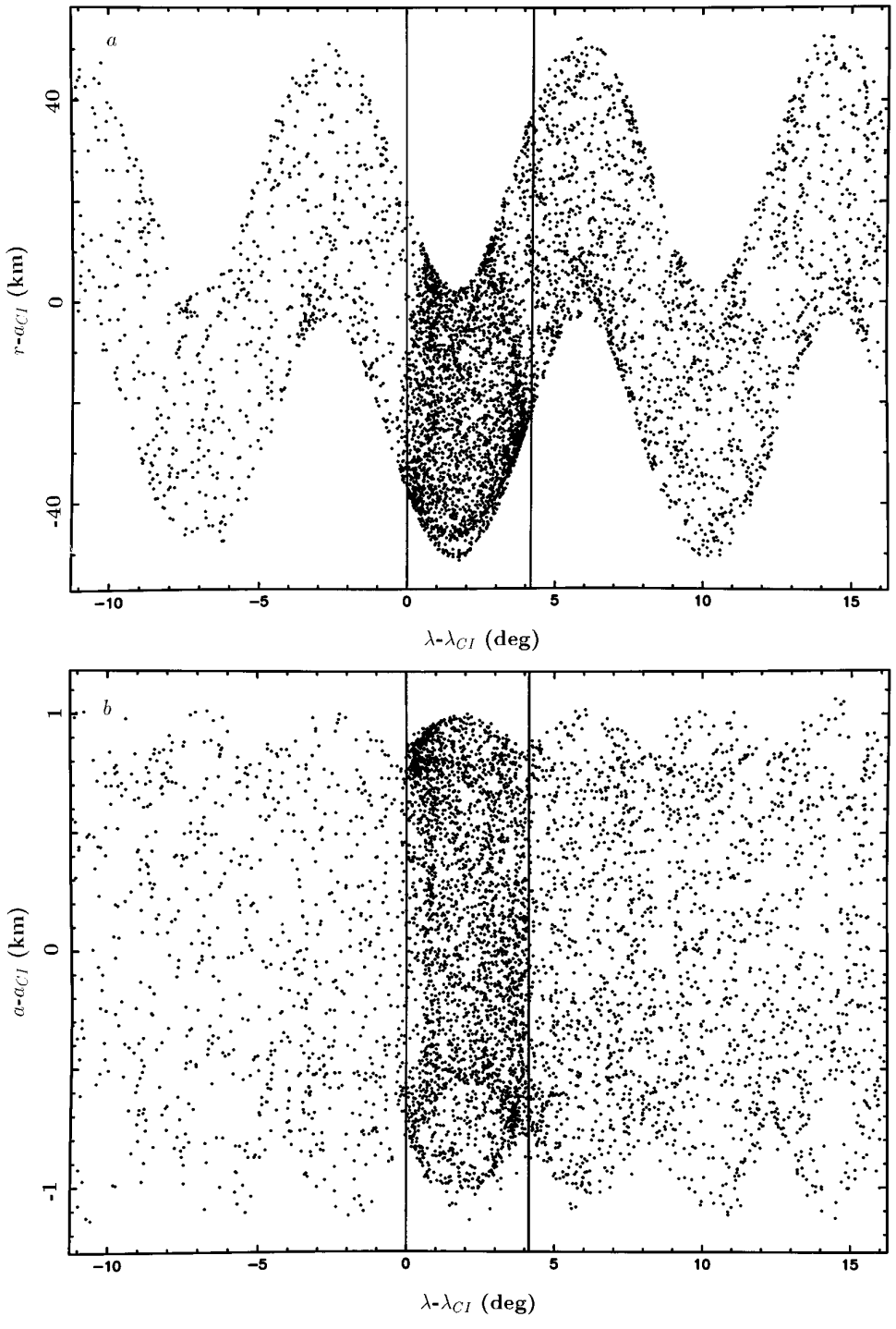

FIG. 11. Same as described in the legend to Fig. 10, but with 10^4 particles initially released from particle 2 of Fig. 8. *No dissipation is applied*. The system is shown after 450 years. In this figure and in those following, the vertical lines mark the boundaries of the corotation site where the particles are initially released. (a) Positions of the particles in a longitude-radius diagram. An arc is still clearly visible around the parent body. Many particles have escaped the site, forming a continuous ring of width ~50 km. The structure of the latter is examined more globally in Figs. 15 and 16. The sine-shaped structure of amplitude ~30 km is forced by the nearby Lindblad resonance (see Eq. (11)). (b) Positions of the guiding centers of the particle motion in a longitude-semi-major axis diagram. Note the change of scale between (a) and (b). Although stably trapped in the site, the particles have semi-major axes spanning a radial interval quite larger than the expected width of the corotation site ($W_{\rm CI} \sim 0.5$ km, see Eq. (9)). This behavior has already been illustrated in Fig. 4 and is discussed in Section 5.2. (c) Azimuthal density distribution. Note the structures inside the arc, with the accumulations of material near the separatrixes with adjacent sites (vertical lines). This is caused by the slower libration motion of the particles there. Note also the absence of clear structures in the continuous part of the ring. (d) Mutual inclinations $I_{\rm m}$ of the particles and the satellite vs longitude.

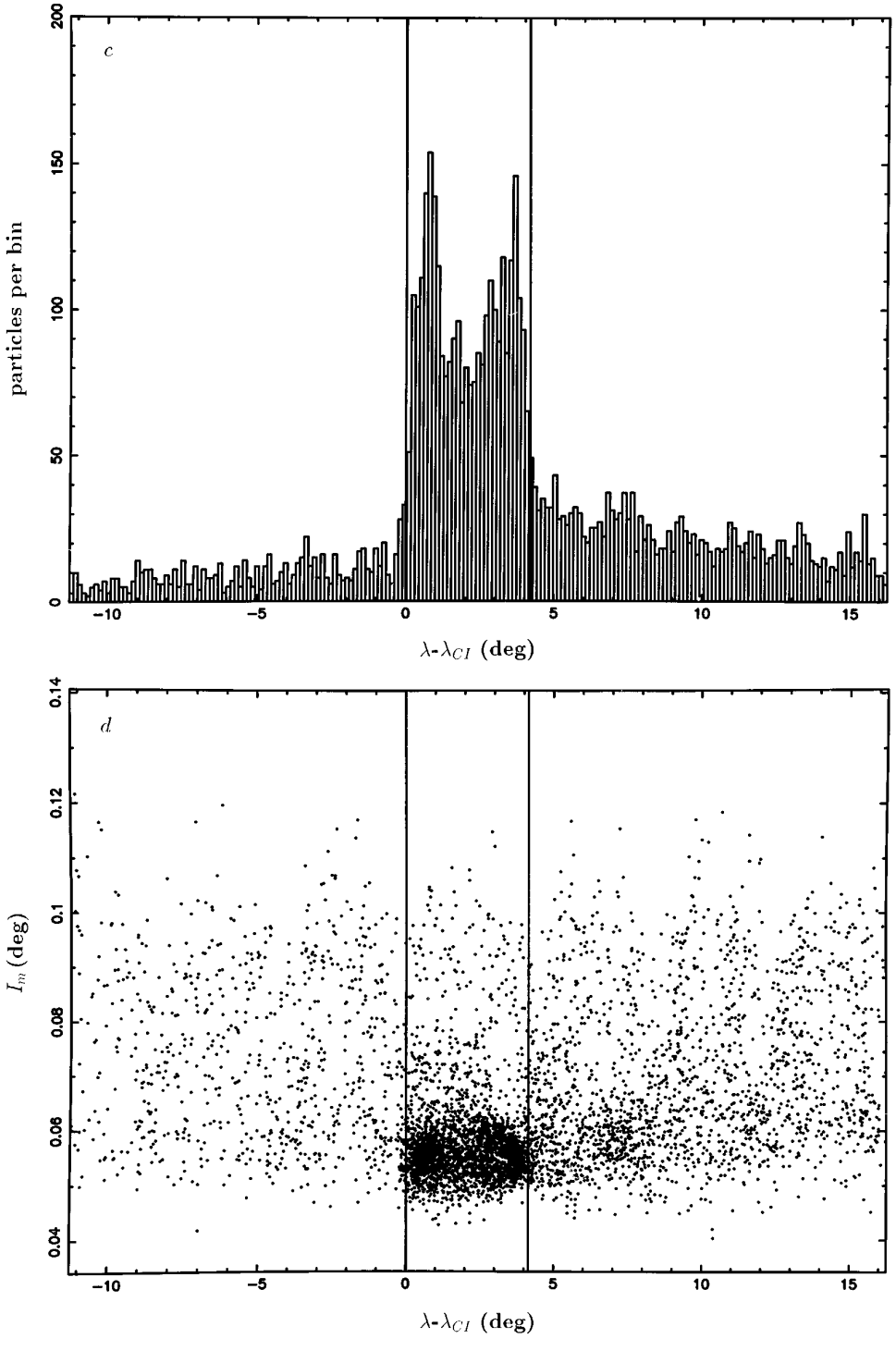

FIG. 11—*Continued*

"parent body" (particle 1, 2, or 3 of Fig. 8), but with a certain velocity dispersion with respect to that body.

More precisely, these 10^4 particles have relative velocities randomly distributed in the 3-D space, with a modulus randomly chosen between 0 and $v_{\max} = 1$ cm sec^{-1}. This ejection velocity can be the result of a collision by another body. We have chosen a typical value of $v_{\max} = 1$ cm sec^{-1} because, for larger velocities, the particles leave rapidly the arc region, especially under the effect of Poynting–Robertson drag (Section 8.2). On the other hand, smaller values of $v_{\max}$ would give very similar initial conditions, and thus would yield little information on the spreading

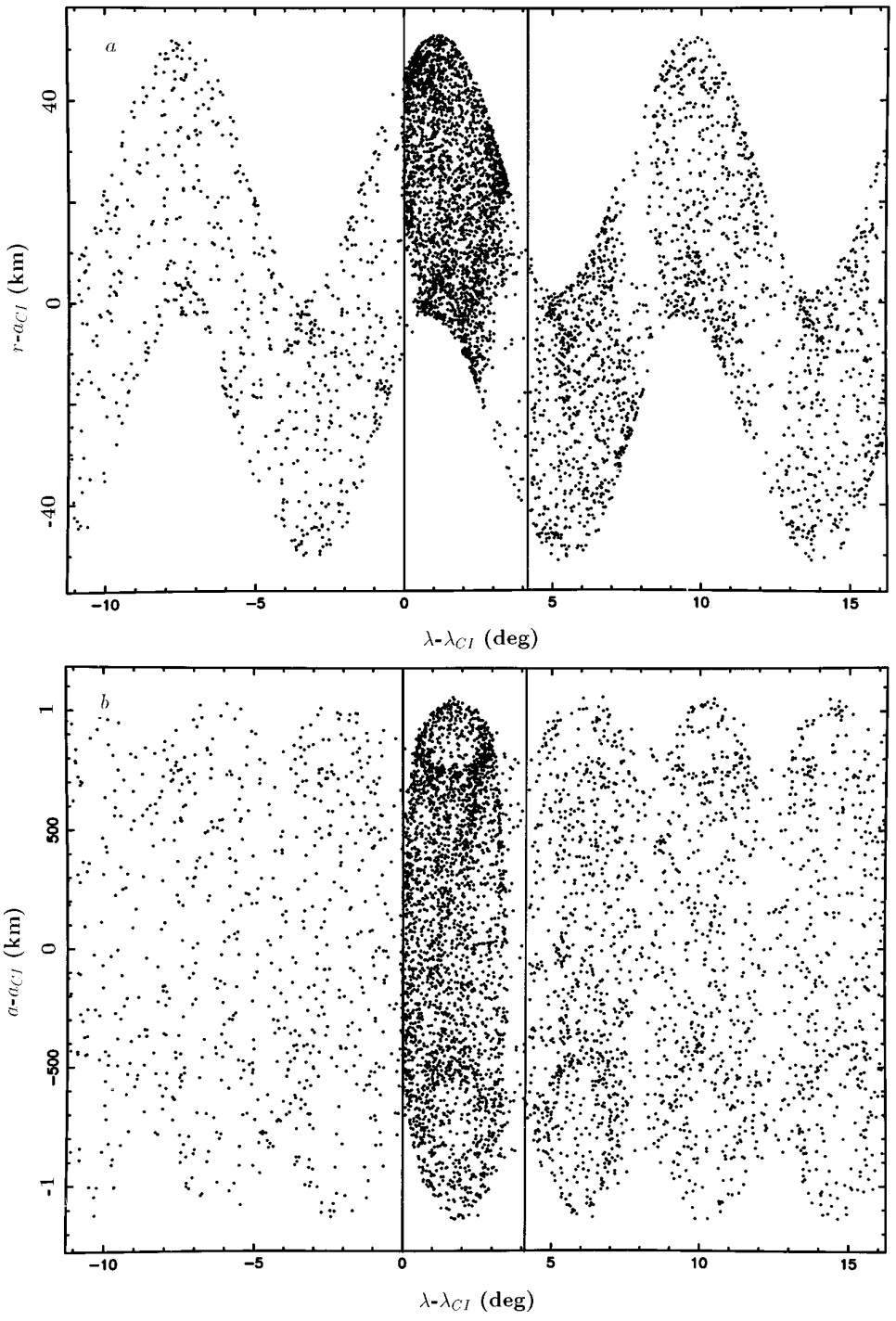

FIG. 12. Same as described in the legend to Fig. 11, but after 500 years. At that time, the arc particles are reaching their maximum values of I_m, see (d). This explains why they are more efficiently confined in the arcs. Compare in particular the conspicuous arc structures observed in (c) and the corresponding Fig. 11c.

of the cloud of particles. Thus, the value of v_{max} taken here is justified as long as we want to know how particles ejected from a parent body will fill in the corotation sites.

Figure 10 shows the positions of particles ejected from particle 3, after 500 years of integration ($\sim 4 \times 10^5$ revolutions). All the particles remain trapped in the corotation site. As the parent body gets closer to the separatrix, however, the ejected particles can escape from the site. Examples are given in Figs. 11 and 12, corresponding to ejection of dust from particle 2. Note the continuous component

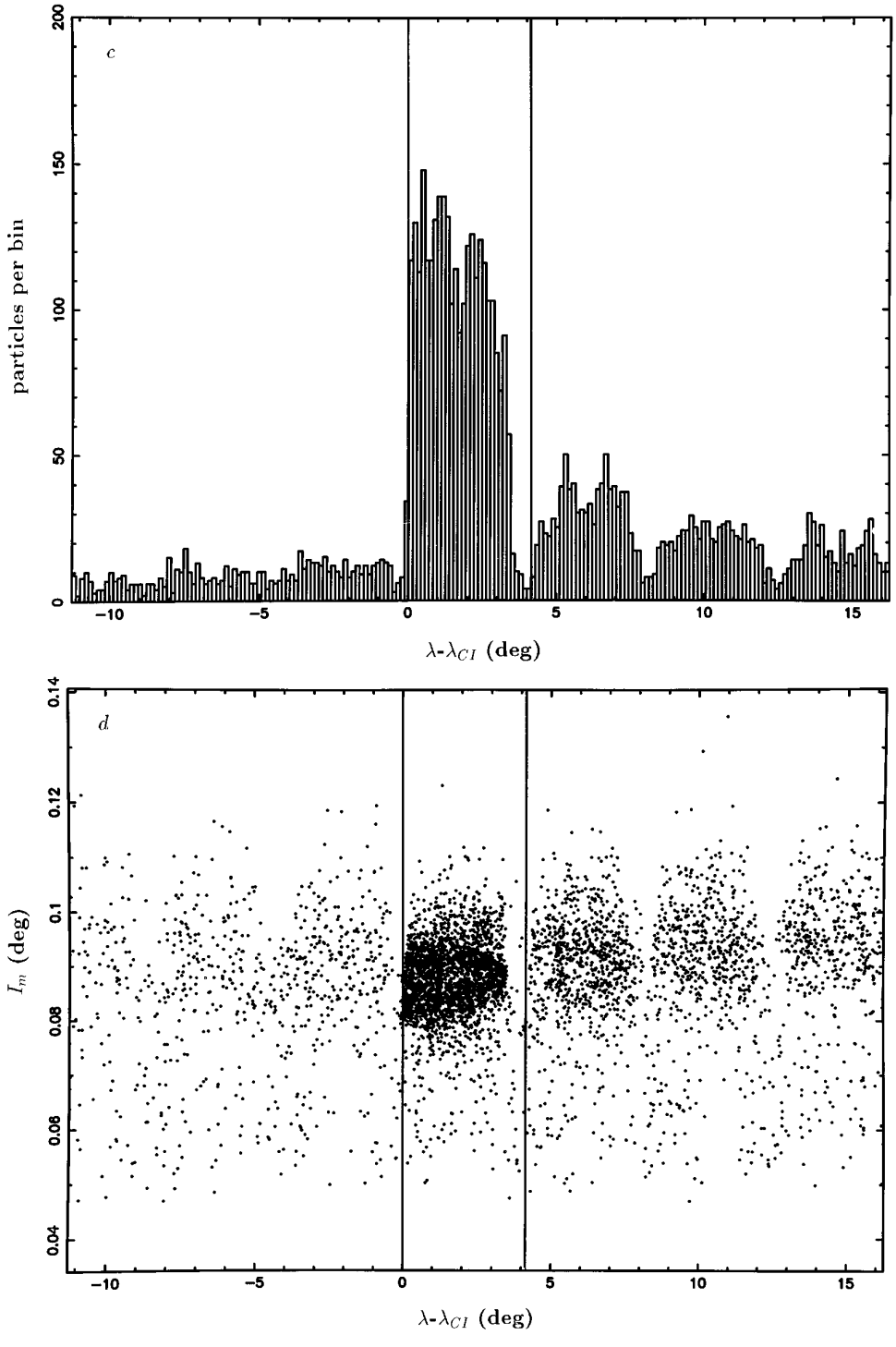

FIG. 12—*Continued*

of the ring created by the particles which have escaped from the site. Note also that the arc remains nevertheless well defined, although its azimuthal structure may vary in time (compare Figs. 11c and 12c).

In Fig. 11c, particles statistically *accumulate* near the two separatrixes, due to the slower azimuthal drift rate near the saddle points connecting adjacent sites (vertical lines). Note also that the border with the site just right of the main arc is not well defined. This is because particles are migrating to that adjacent site. This migration is correlated with the mutual inclinations $I_{\rm m}$ of the arc particles and the satellite being minimum, see Fig. 11d. In Fig. 12c, in

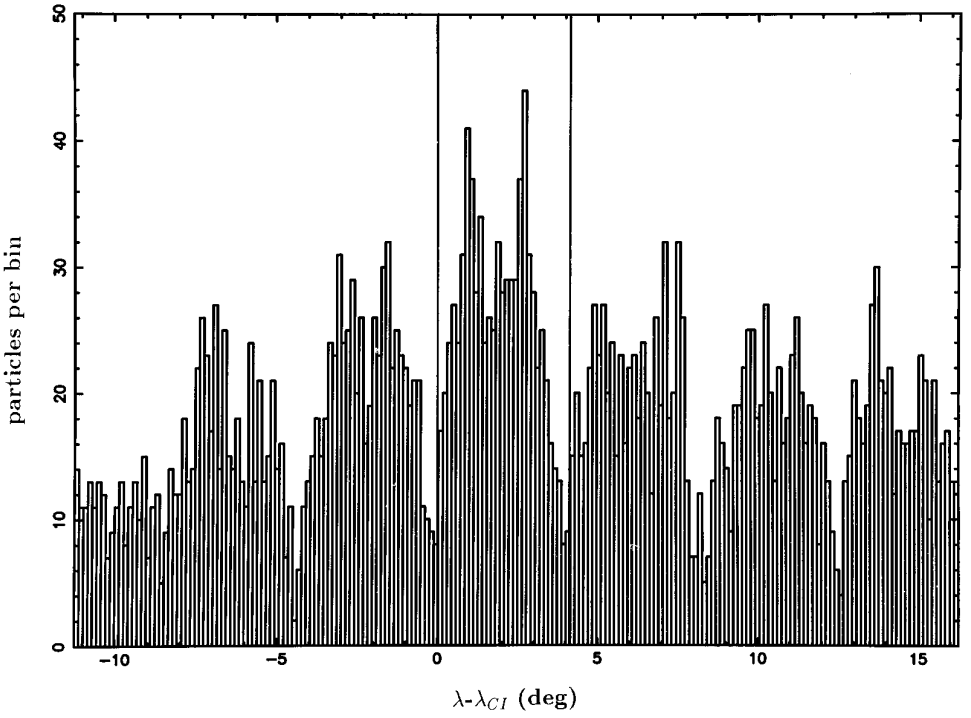

FIG. 13. Same as described in the legend to 12c, but with 10^4 particles initially released from the particle 1 of Fig. 8. The system is shown after 500 years. The initial arc region (delimited by vertical lines) is still visible, but will be rapidly erased by ongoing migrations from site to site.

contrast, the main arc is much better defined. The borders at the left and the right of this arc are quite sharp. Correspondingly, the mutual inclinations I_m are at their maxima (Fig. 12d), so that no migrations to neighbor sites are taking place.

In the last run of this series, particles are ejected from particle 1. Because this particle is closest to the separatrix, compared to particles 3 and 2, more escapes take place. After 500 years (Fig. 13), most of the particles have left the initial site and have populated the neighbor sites. Although the signatures of the various arcs are still visible, these structures will rapidly disappear due to the mixing of particles from site to site.

In all the diagrams showing the position of the particles, it is interesting to note that the physical width of the arcs (~50 km) is quite *larger* than the width expected from the eccentricity gradient caused by the LER across the arc, ~7 km (see Section 5.1). Clearly, this is due to the fact the particles do not have initially the forced eccentricity given by Eq. (11). Instead, they follow more complicated trajectories, an example of which is given in Fig. 4. The implications of this effect for the arc stability are discussed in Section 10. We note for the moment that this relatively large width is maintained during one revolution of the arcs (~10.5 hr), as illustrated in Fig. 14. This figure shows a sequence of six images taken every 2 hr, covering 10 hr. As we discuss in Section 9, the particles at the outer part of the arcs at a given time will cross the trajectories of particles at the inner part every half period, resulting in collisions.

7.3. Azimuthal Structure of the Arcs

We now examine some interesting azimuthal structures caused by the stochastic migration of the particles between sites. Once again, it is important to note that these structures appear *without any dissipative processes;* i.e., they are solely due to the chaotic nature of the gravitational perturbations of the satellite. In that sense, the structures we will describe concern the larger particles of Adams ring (parent bodies), from which dust can be ejected.

Figure 15 presents a general pole-on view of the ring already shown in Fig. 12. One can see the radial forcing due to the LER (exaggerated by a factor 100 for sake of clarity), the clustering of particles around the parent body (particle 2), as well as the continuous component due to those particles which escaped the initial corotation site.

A close up view of the parent body region is shown in Fig. 15b. One can note the dense arc, accompanied by three fainter leading arcs (already visible in Fig. 12c). Finally, a global azimuthal density profile of the ring is shown in Fig. 16. One can note the densely populated arc region, and also the general bowl-shaped ring profile which reaches a minimum 180° away from the densest region. This is

reminiscent of the density profile observed in Adams ring (Showalter and Cuzzi 1992).

More complicated patterns can be generated, as shown in Fig. 17. Several groups of particles were released from different parent bodies, at various locations and at different moments. In the example shown in Fig. 17, six releases of particles have been triggered during the 500 years of the simulation (one at the initial time, and the most recent one 250 years later). The times and locations of these releases were chosen to crudely reproduce the azimuthal profile of Adams ring arcs, with Liberté, Egalité, and Fraternité. Note in particular the trailing arc spanning two corotation sites, between the longitudes $\sim 5°$ and $\sim 13°$, which is reminiscent of arc Fraternité. This phenomena is actually due to the merging of two previously isolated arcs.

Of course, the choice of the times and the locations where the particle were released are completely *ad hoc,* since they are intended to reproduce the present structure of Neptune's arcs system. Nevertheless, this shows at least that it is *possible* to reproduce this general structure, using only random events. A more complete study must of course take into account much more complex processes, such as drag forces (Poynting–Robertson or even a planet exosphere) or collisions. Some aspects of these processes are now examined.

8. RADIATION FORCES

We address here the question of the arc stability against radiation forces. We are thus concerned now with the population of $\sim$1–100 μm-sized particles. These forces can be divided in two classes: the pressure of radiation and the Poynting–Robertson (PR) drag. An exhaustive description of these forces and their effects can be found in Burns, Lamy, and Soter (1979), thereafter referred to as BLS.

Each of these forces arises from two sources: the Sun and Neptune. Their intensity is conveniently expressed in terms of the ratio $\beta_\odot$ (β_N) between the radiation pressure $F_P(\odot)$ ($F_P(N)$) due to the Sun (Neptune) and the gravitational force $F_G(\odot)$ ($F_G(N)$) due to the Sun (Neptune). Each β depends on the optical properties of the grain and of the source of light. We shall see that the planetary contribution (β_N) can actually be neglected in our case. For spherical particles of radius s and density ρ illuminated by the Sun, BLS obtain

$$\beta_\odot \sim 0.57 Q_\odot \left(\frac{1\ \mathrm{g\ cm^{-3}}}{\rho}\right)\left(\frac{1\ \mu\mathrm{m}}{s}\right), \tag{20}$$

where $Q_\odot$ is the radiation pressure efficiency for the solar light. Unless otherwise stated, when numerical applications are required, s and ρ will respectively be expressed in micrometers and grams per centimeter^3. We will discuss the results in terms of $\beta_\odot$, the conversion to the particle size being provided by the equation above.

8.1. Pressure of Radiation

The pressure of radiation $F_P(\odot)$ due the Sun is $f_\odot A Q_\odot / c$, where $f_\odot$ is the solar constant at the particle, A is its geometrical cross-section, and c is the speed of light. The same expression holds for the planetary pressure of radiation $F_P(N)$, with subscripts N instead of $\odot$. Thus,

$$\frac{F_P(N)}{F_P(\odot)} = \left(\frac{f_N}{f_\odot}\right)\left(\frac{Q_N}{Q_\odot}\right). \tag{21}$$

We have $f_N/f_\odot \sim p(R_N/a)^2$, where the geometrical albedo of Neptune is $p \sim 0.3$, its radius is $R_N \sim 25{,}000$ km, and the distance to the planet is $a \sim 63{,}000$ km, so that $f_N/f_\odot \lesssim 0.05$. If we consider the solar reflected light from Neptune, then $Q_N = Q_\odot$. If we consider the IR emission of the planet (at 50 μm and larger wavelengths), then $Q_N \ll Q_\odot$ because the wavelength becomes larger than the particles. In any case, we see that $f_P(N)/f_P(\odot) \ll 1$. The pressure of radiation of the Sun thus dominates by far that of the planet.

Strictly speaking, however, the effect of the pressure of radiation from Neptune is to replace the mass of the planet by $(1 - \beta_N)M_N$. This in turn shifts the location of a given resonance by $\delta a = a\beta_N/3$, from Kepler's third law. Even if this effect is not dominant compared to the solar pressure of radiation, it should be quantified, especially because of the close packing of the resonances (Fig. 1). We have

$$\frac{\beta_N}{\beta_\odot} = \left(\frac{f_N}{f_\odot}\right)\left(\frac{Q_N}{Q_\odot}\right)\left(\frac{F_G(\odot)}{F_G(N)}\right). \tag{22}$$

Using the typical values of the gravitational forces $F_G(N)$ and $F_G(\odot)$ at Adams ring, one gets $\beta_N/\beta_\odot < \sim 2 \times 10^{-7}$. Finally, from Eq. (20), one obtains $\beta_N < \sim 10^{-7} Q_\odot/\rho s$. Even for $s = 1$ μm, $Q_\odot = 1$, and $\rho = 1$ g cm^{-3}, we see that $\beta_N < \sim 10^{-7}$. Thus, the pressure of radiation from the planet causes, at most, a shift of the resonance radius of $\delta a \sim 2$ m. In view of other, quite larger, perturbations, this shift can be neglected here. Note also that the nightside asymmetry has not been considered here, since the planetocentric elevation of the Sun is presently large enough for the Adams ring to be permanently illuminated by the solar light.

Introducing the pressure of radiation $F_P(\odot)$ due to the Sun is a more arduous task, at least from an analytical point of view. Its effects have been extensively described by Mignard (1982, 1984) and Mignard and Hénon (1984). They showed that in the case of a spherical planet, the

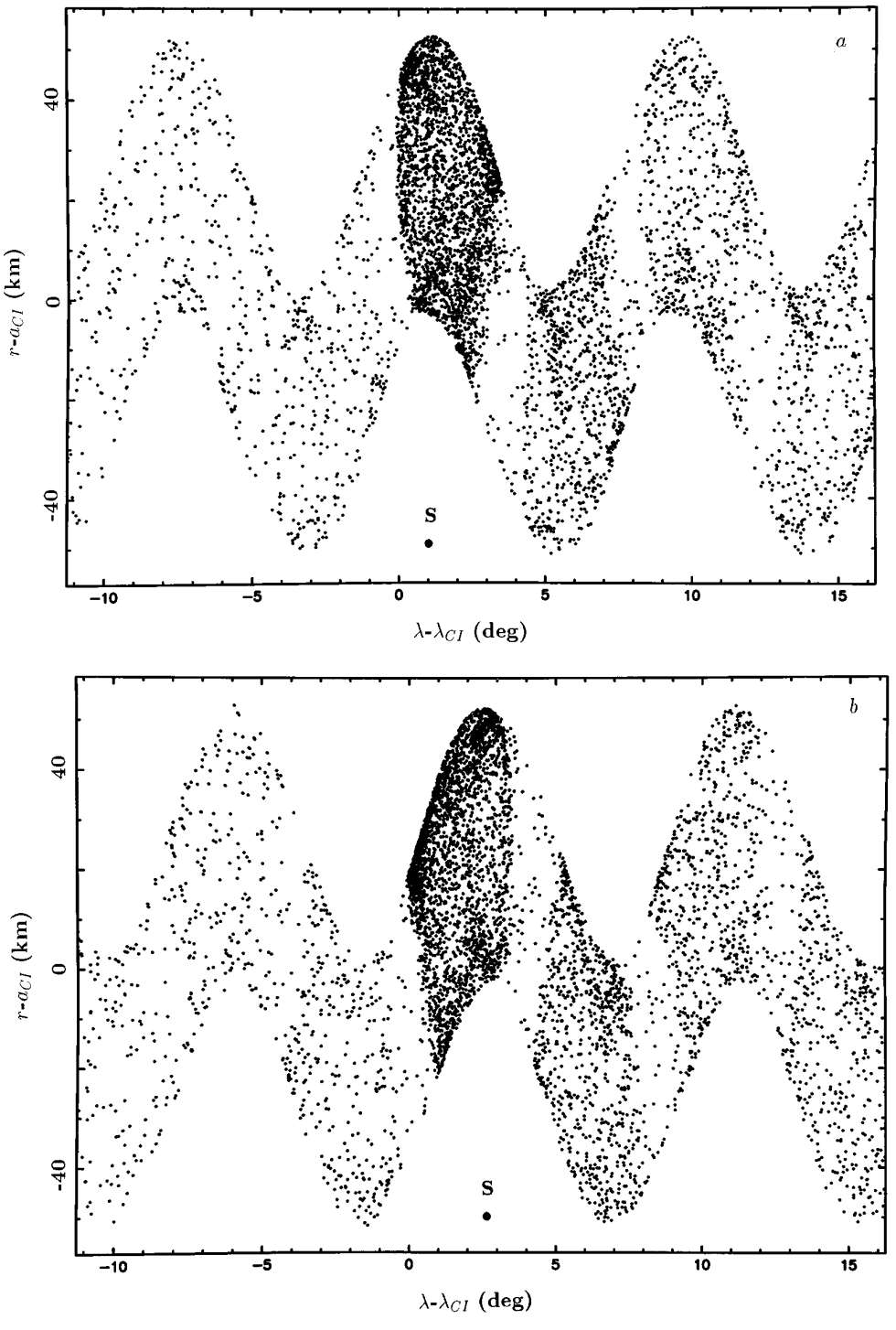

FIG. 14. (a) Same as described in the legend to Fig. 12a. (b)–(f) Positions of the particles every 2 hours. The total time span, 10 hours, represents approximately one orbital revolution of the arc (~10.5 hr). In this frame, corotating with the corotation site, the arc keeps a constant longitude. The general sine-shaped structure, on the other hand, is forced by the LER and follows the satellite. The longitude of the satellite (but *not* its real radial position) is marked by the dot labeled *S*.

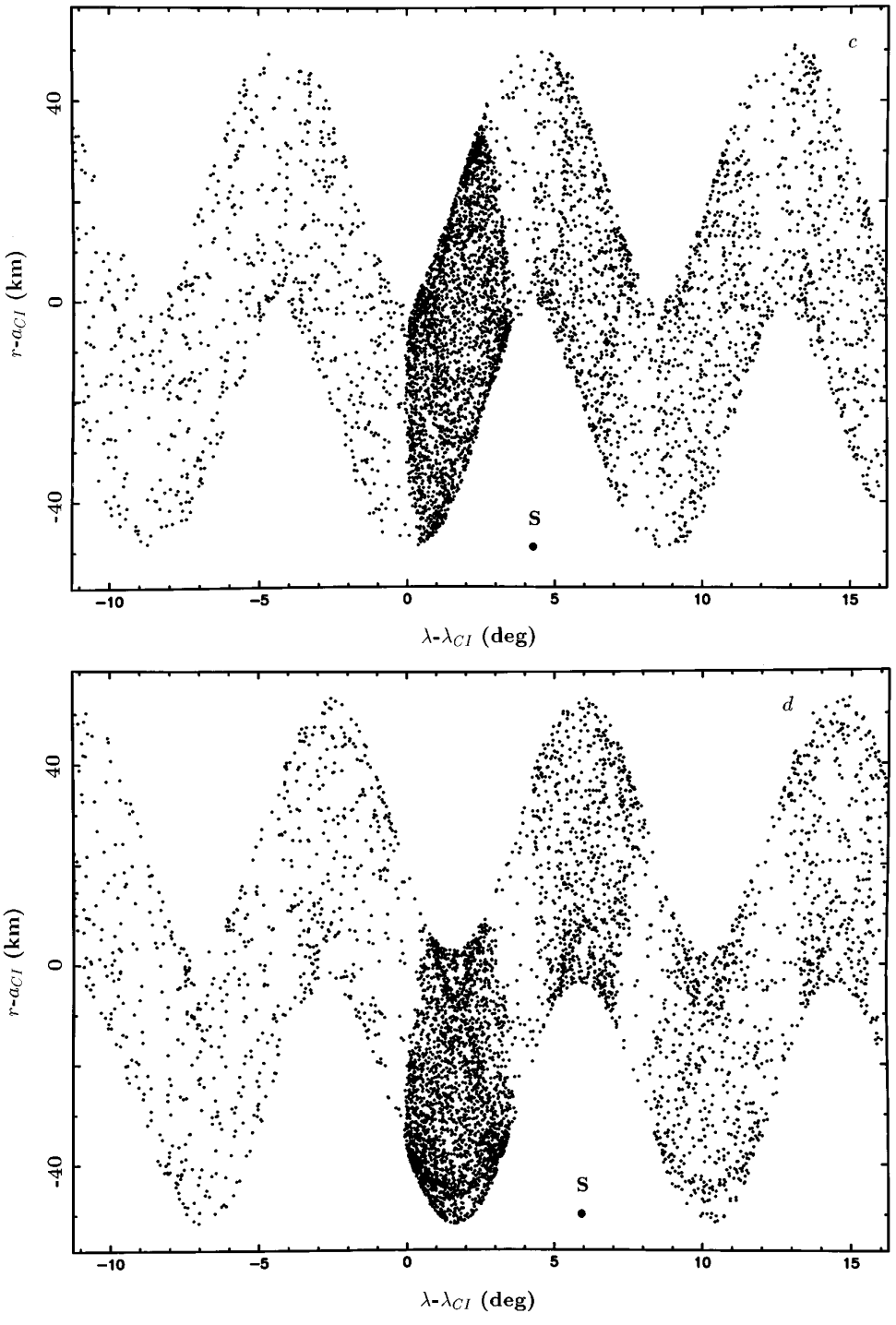

FIG. 14—*Continued*

problem is integrable. In particular, the semi-major axis of the particle is conserved, but quite large eccentricities can be forced. In the case of an oblate planet, however, the eccentricity forced by $F_P(\odot)$ is very much reduced, essentially due to the fast precession rate induced on the periapse. Instead of taking an analytical approach, we have used in our numerical code the perturbation equations derived by Hamilton (1993). His equations (10a)–(10e) provide the rates of change of the particle orbital elements caused by $F_P(\odot)$.

We consider again the particle 3 of Fig. 8, but now, it is submitted to the solar pressure of radiation. We have

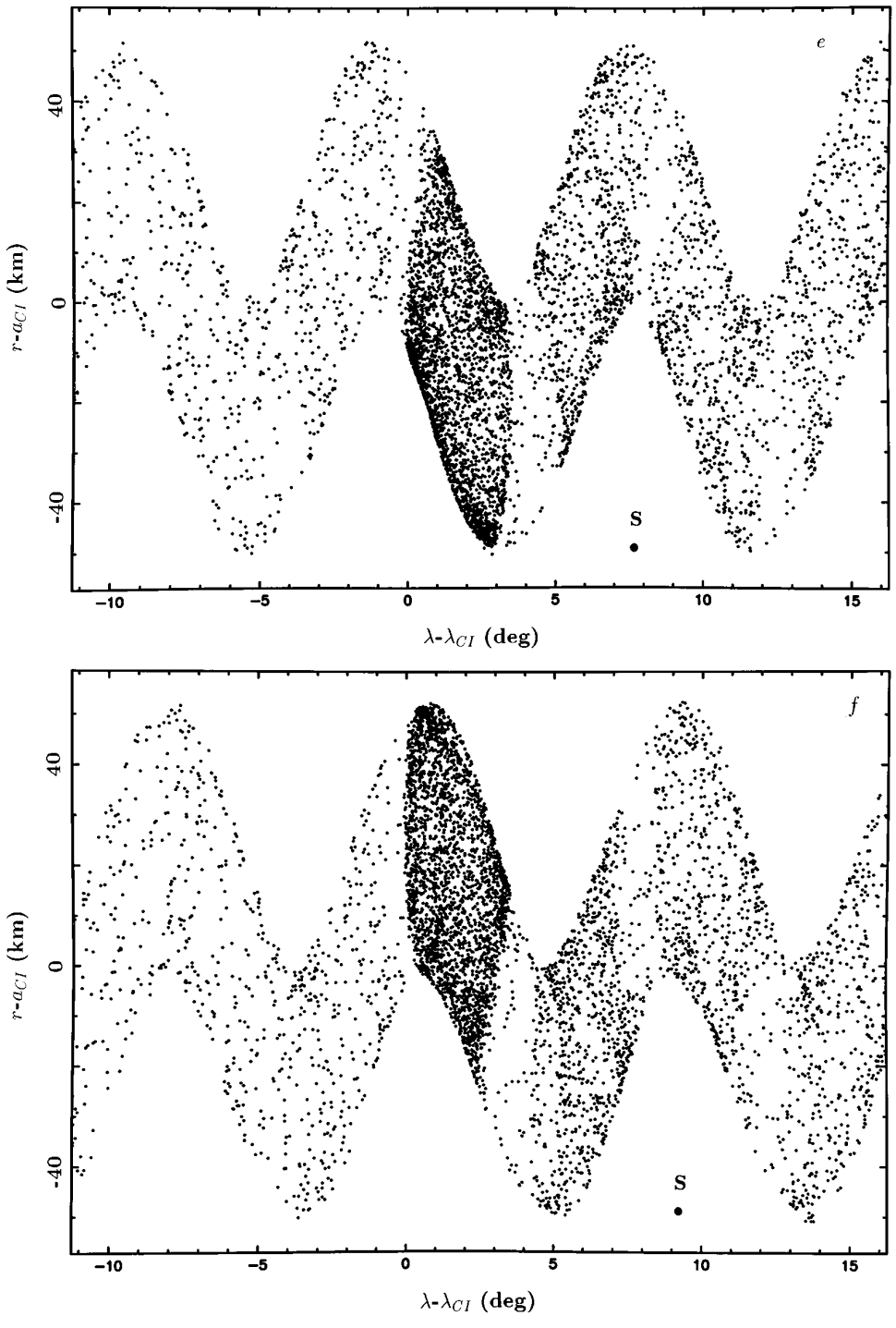

FIG. 14—*Continued*

taken various values for the coefficient $\beta_\odot$, namely 0.2, 0.02, 0.004, and 0.002. Considering a rocky particle with a density $\rho = 3$ g cm^{-3} in the geometrical optics approximation ($Q_\odot = 1$), Eq. (20) yields corresponding particle sizes of $s = 1$, 10, 50, and 100 μm, respectively.

Figure 18 shows the motion of the particle in the corotating frame, for 500 years. Particles with $\beta_\odot > \sim 0.01$ are blown away from the corotation sites in a few years only, although some transient captures in other sites may occur subsequently.

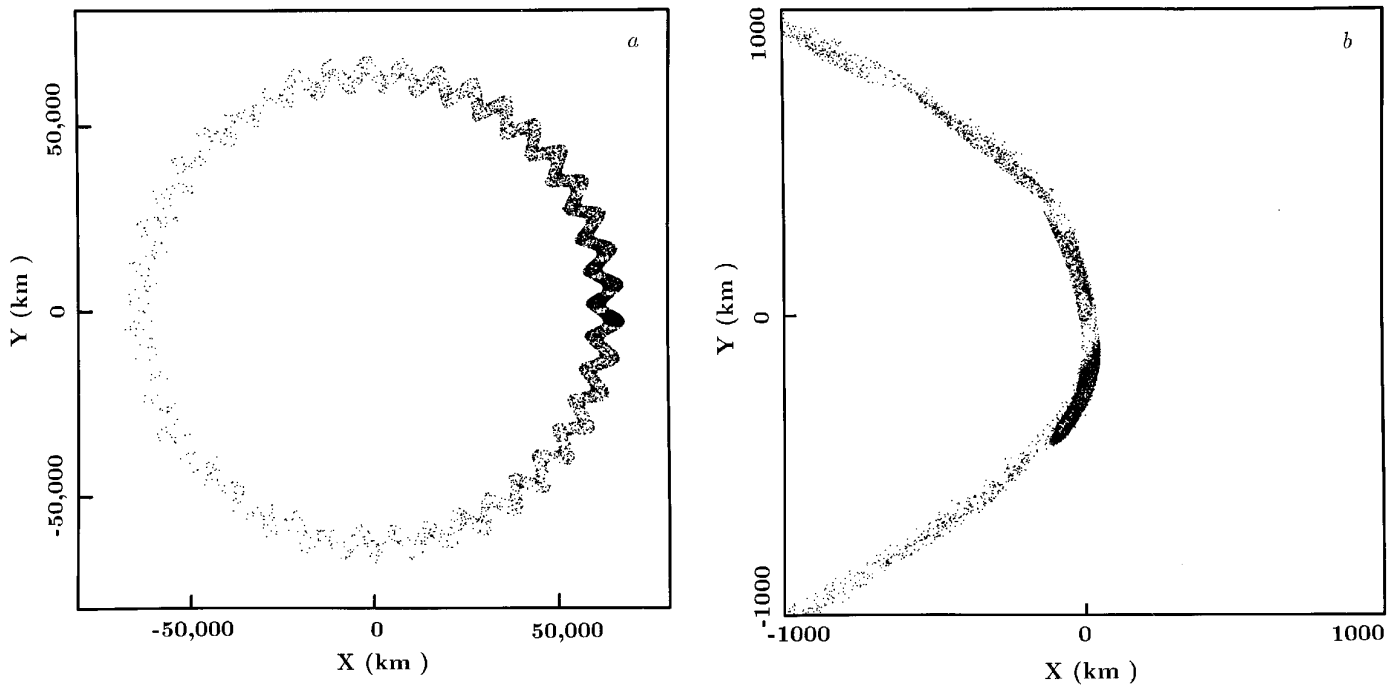

FIG. 15. (a) Complete pole-on view of the simulation already shown in Fig. 12. For sake of clarity, the radial distorsion of the ring has been expanded by a factor 100 with respect to the CIR radius. Note the gradual fading of the ring density as one gets away from the initial arc region. (b) Close-up view of the arc region, as observed from an elevation of 5° above the ring plane. Note the finite width of the ring.

8.2. Poynting–Robertson Drag

Like the pressure of radiation, the PR drag arises from both Neptune and the Sun. Each source creates a dissipative force, namely $\mathbf{F}_{\mathrm{PR}}(\mathrm{N}) = -\beta_{\mathrm{N}} F_{\mathrm{G}}(\mathrm{N})\mathbf{v}/c$ and $\mathbf{F}_{\mathrm{PR}}(\odot) = -\beta_{\odot} F_{\mathrm{G}}(\odot)\mathbf{v}/c$, where $\mathbf{v}$ is the orbital velocity of the particle around Neptune. Again we have $F_{\mathrm{PR}}(\mathrm{N})/F_{\mathrm{PR}}(\odot) = (f_{\mathrm{N}}/f_{\odot})(Q_{\mathrm{N}}/Q_{\odot}) \ll 1$. Consequently, only the solar PR drag will be considered here.

In the limiting case where the eccentricity is zero, the PR drag damps the semi-major axis and orbital eccentricity of the particle at rates (BLS):

$$\left(\frac{1}{a}\frac{da}{dt}\right)_{\mathrm{PR}} = -\frac{4}{5}\alpha_{\odot} \tag{23}$$

$$\left(\frac{1}{e}\frac{de}{dt}\right)_{\mathrm{PR}} = -\alpha_{\odot}, \tag{24}$$

with $\alpha_{\odot} = \beta_{\odot}\,(5GM_{\odot})/(2ca_{\odot}^2) \sim 5.5 \times 10^{-14}\beta_{\odot}\ \mathrm{sec}^{-1}$, where $M_{\odot}$ and $a_{\odot}$ are the mass and distance of the Sun, respectively. At the radius of Adams ring, this implies a decay rate of $(da/dt)_{\mathrm{PR}} \sim -110\beta_{\odot}$ m year^{-1}. At first glance, this seems quite a rapid decay. For instance, a particle with $s = 1\ \mu$m, $Q_{\odot} = 1$, and $\rho = 1$ g cm^{-3} would cross the entire corotation site in less than 8 years. However, the CIR and LER resonances interact with the PR drag, allowing the particle to reach an equilibrium configuration. The damping rates given in Eqs. (23) and (24), combined with the system (16), provide the new system:

$$\begin{aligned}
\frac{d\chi}{d\tau} &= +3m^2[2\varepsilon_{\mathrm{i}} I_{\mathrm{s}}^2 \sin(\Psi_{\mathrm{CI}}) + \varepsilon_{\mathrm{e}} k] - \frac{6\alpha_{\odot}}{5n} m \\
\frac{d\Psi_{\mathrm{CI}}}{d\tau} &= +2\chi \\
\frac{dh}{d\tau} &= -(\chi + j_{\mathrm{p}})k \qquad\qquad -\frac{\alpha_{\odot}}{n} h \\
\frac{dk}{d\tau} &= +(\chi + j_{\mathrm{p}})h - \varepsilon_{\mathrm{e}} \qquad -\frac{\alpha_{\odot}}{n} k.
\end{aligned} \tag{25}$$

Inside a corotation site, an equilibrium is possible at the point

$$\begin{aligned}
\sin(\Psi_{\mathrm{CI}}) &\sim \frac{\alpha_{\odot}}{5mn\varepsilon_{\mathrm{i}} I_{\mathrm{s}}^2} \sim -0.52\beta_{\odot} \\
\chi &= 0 \\
h &= \frac{j_{\mathrm{p}}\varepsilon_{\mathrm{e}}}{(\alpha_{\odot}/n)^2 + j_{\mathrm{p}}^2} \sim \frac{\varepsilon_{\mathrm{e}}}{j_{\mathrm{p}}} \\
k &= \frac{-(\alpha_{\odot}/n)\varepsilon_{\mathrm{e}}}{(\alpha_{\odot}/n)^2 + j_{\mathrm{p}}^2} \sim 0,
\end{aligned} \tag{26}$$

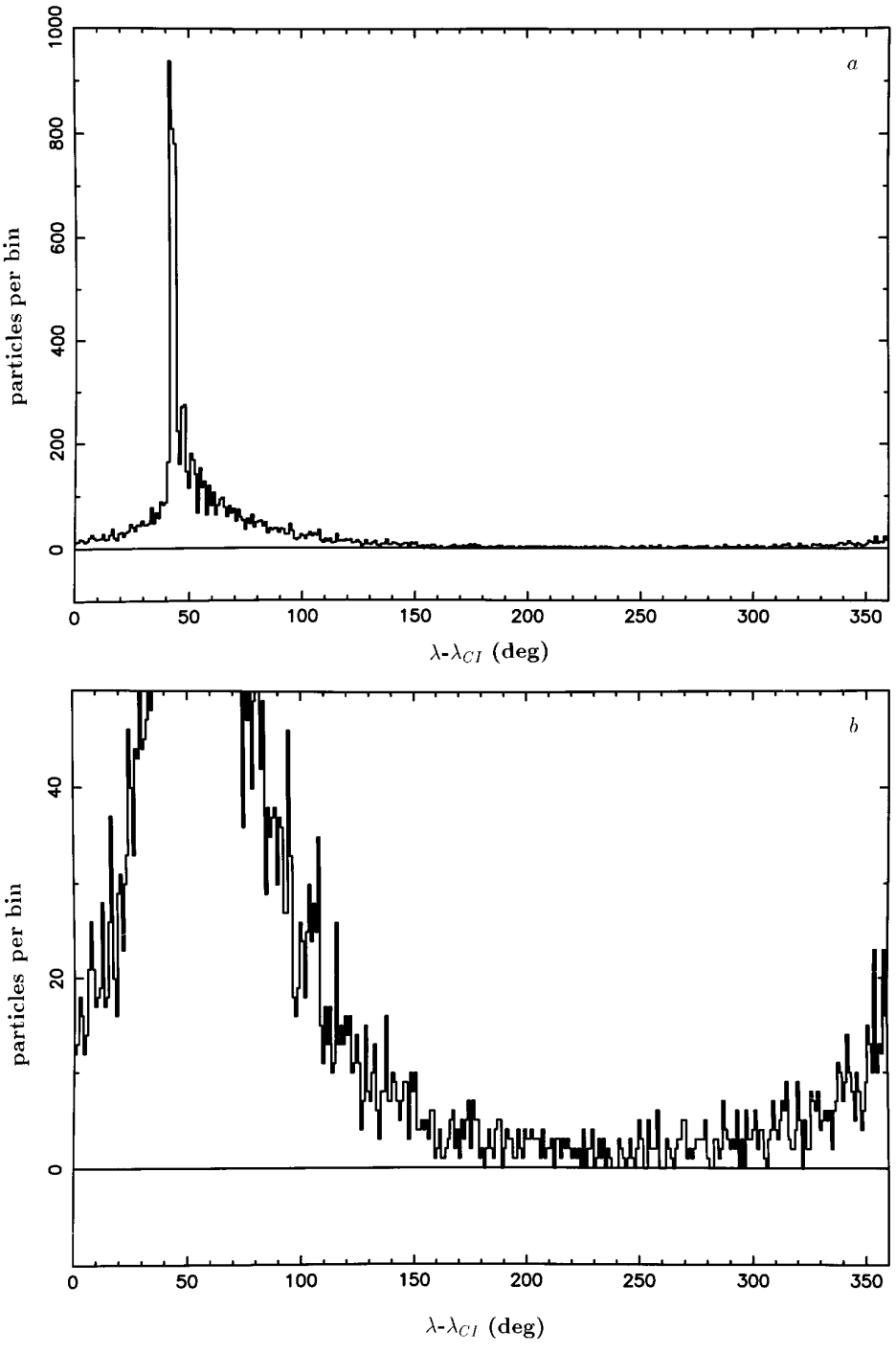

FIG. 16. Azimuthal distribution of the particles shown in the previous figure. (a) General view showing the main arc and the leading secondary arcs. (b) Vertically expanded view showing the overall bowl shape of the continuous ring component, with the minimum reached 180° away from the arc region. Recall this distribution is the result of conservative stochastic diffusion only.

the approximations stemming from the smallness of $\alpha_\odot/n$ with respect to j_p.

Near this equilibrium point, the satellite provides, through the corotation resonance, the energy dissipated by PR drag. One can see that the particle actually remains very close to the equilibrium point corresponding to the conservative case, namely $\Psi_{CI} = 180°$, $\chi = 0$, $h = \varepsilon_e/j_p$, and $k = 0$. For instance, even with the high value of $\beta_\odot = 0.57$ previously used, we get an equilibrium value $\Psi_{CI} \sim 180° + 17°$, corresponding to a shift in longi-

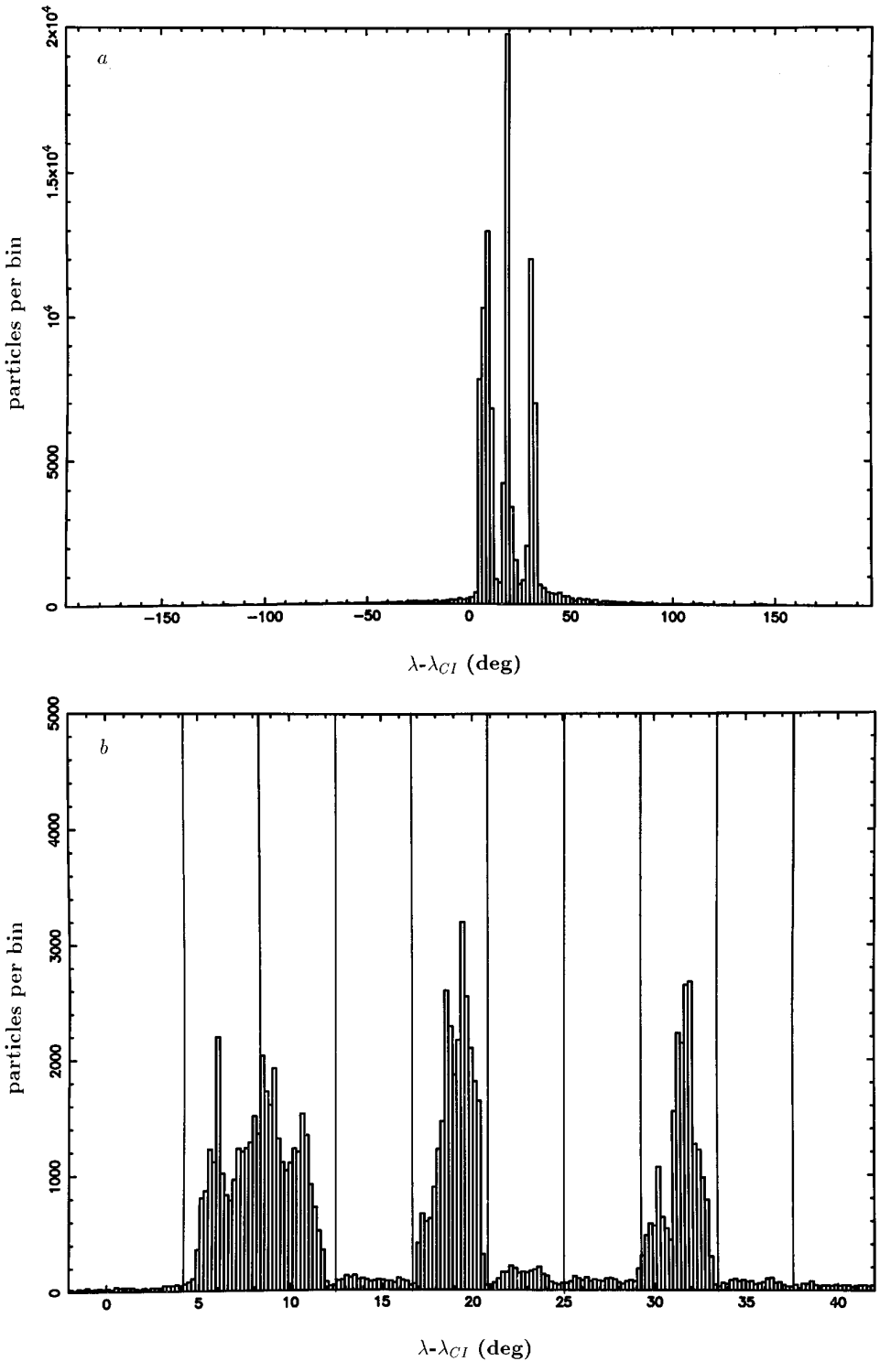

FIG. 17. (a) Azimuthal distribution resulting from the release of 10^4 particles at six different times in a 500-year interval. These times have been chosen so that to crudely reproduce the density azimuthal profile of Neptune's arcs. The vertical lines in the close-up view of (b) delineate the boundaries between corotation sites. See the text for discussion.

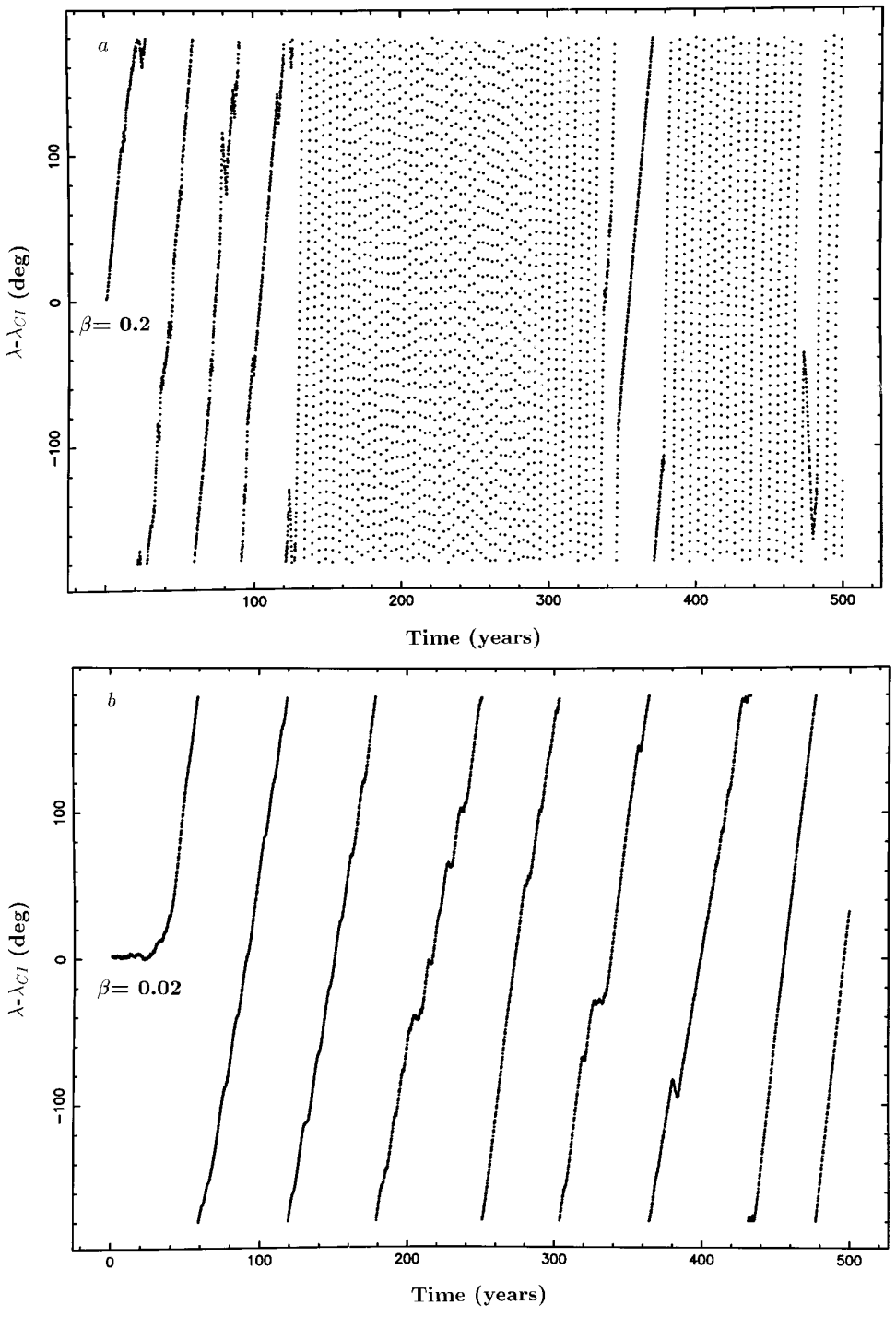

FIG. 18. Mean longitude (in the corotating frame) vs time of a particle subjected to a solar pressure of radiation of various intensities. The initial conditions for that particle is that of particle 3 of Fig. 8. The values of the ratios of the solar radiation pressure to the solar gravity force are as follows: (a) $\beta_\odot = 0.2$, (b) $\beta_\odot = 0.02$, (c) $\beta_\odot = 0.004$, (d) $\beta_\odot = 0.002$. See the text for discussion.

tudes of only $17°/2|m| \sim 0.2°$ with respect to the center of the corotation site.

An example of motion with PR drag (using the mapping, *not* the system (25)) is shown in Fig. 19. The dots represent the positions of the particle guiding center during a 10,000-year integration, with $\beta_\odot = 0.57$. The slow libration motion has a center which is slightly shifted with respect to 180°, as expected from Eq. (26). Figure 20 shows the eccentricity of the particle on a 1000-year time span (lower curve). The eccentricity slowly oscillates around the equilibrium

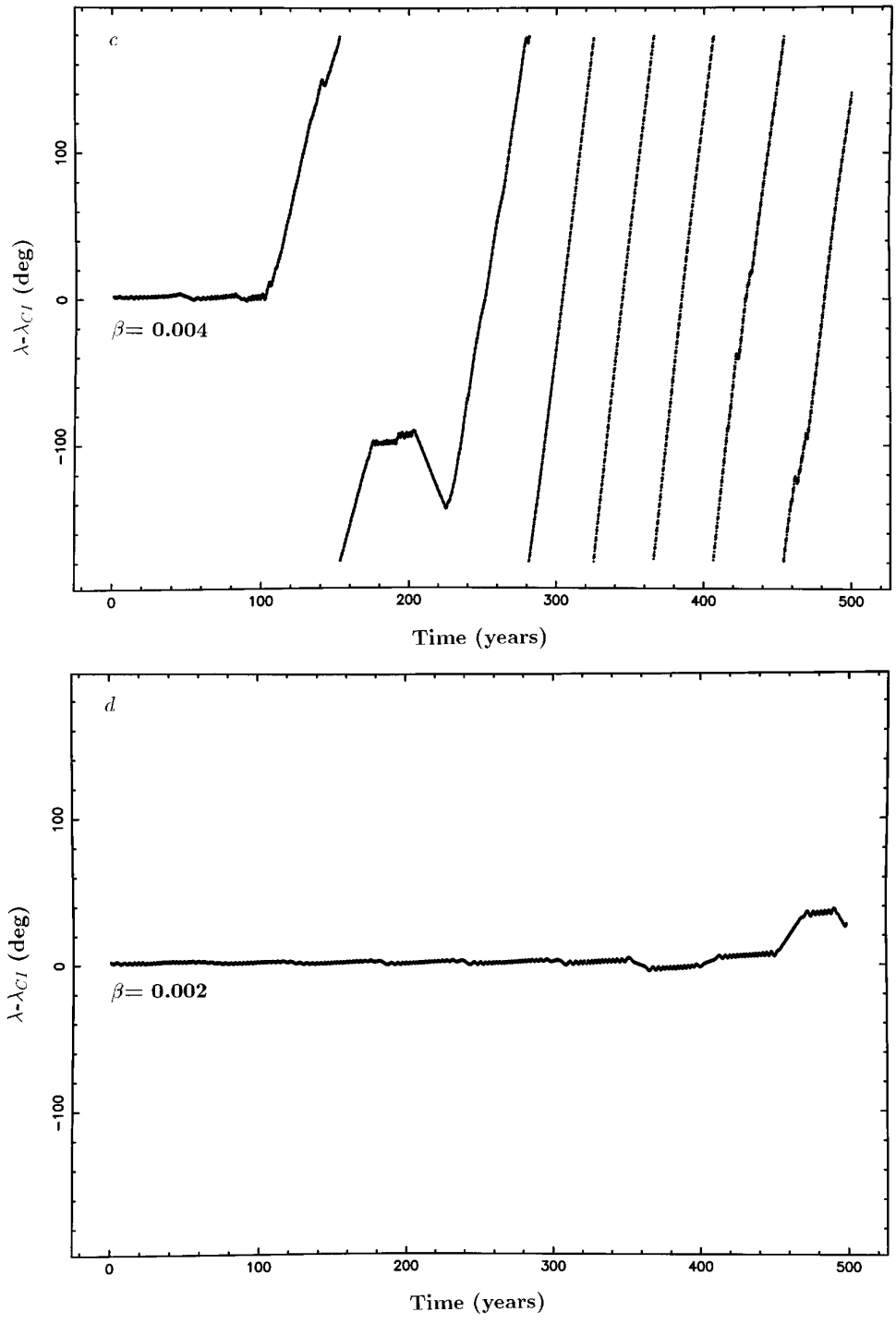

FIG. 18—*Continued*

value $\varepsilon_e/j_p \sim 4.3 \times 10^{-4}$. The oscillations of eccentricity observed in Fig. 20 are expected to damp on a time scale of $1/\alpha_\odot \sim 10^6$ years, according to the system (25). It is thus not surprising that they appear essentially unaltered in these relatively short integrations.

Once a particle escapes from a corotation site, it begins its decay toward the LER radius (1.65 km away) at the rate $\sim -110\beta_\odot$ m year^{-1}. Then, the particle orbital eccentricity is pumped up by the LER, at a rate depending only on $\alpha_\odot$ and m (and *not* on the satellite mass, see Sicardy

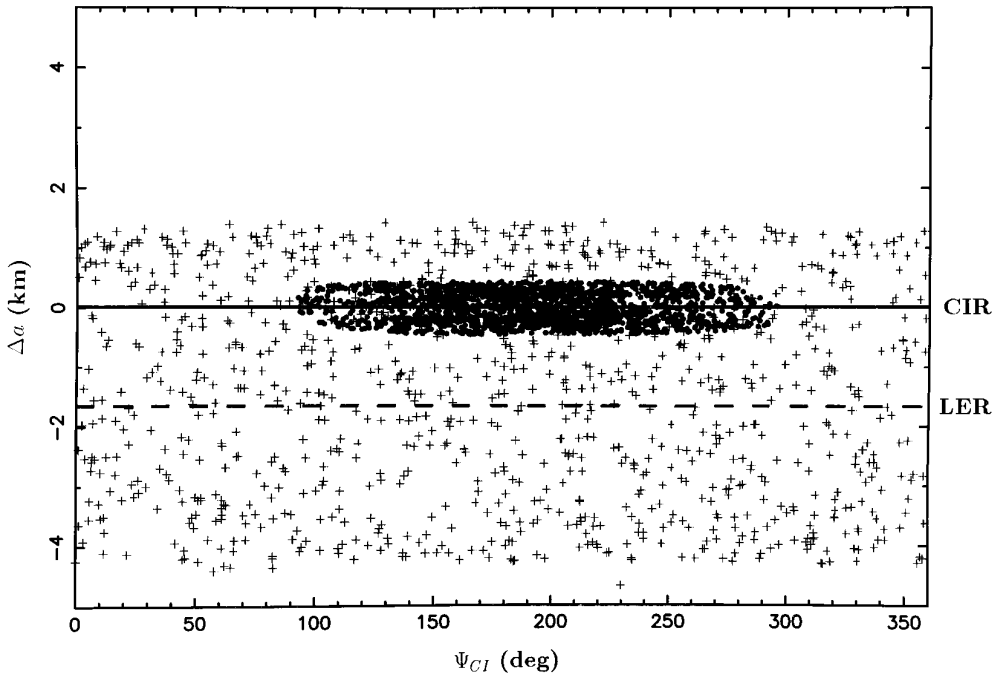

FIG. 19. Stability of an arc particle against the solar Poynting–Robertson drag. Two integrations (using the mapping method) are shown here. In both cases the total time span of each integration is 10,000 years and the ratio $\beta_\odot$ for the particle is 0.57. This value corresponds to an icy 1-μm-sized particle in the limit of geometrical optics. The output shows the guiding center of the particle at successive time steps, namely the distance Δa of the particle guiding center to the CIR radius vs the critical angle $\Psi_{\rm CI}$. Dots: the particle is initially released at the center of the corotation site (CIR radius, $\Psi_{\rm CI} = 0°$, $\Delta a = 0$ km), and then remains stably trapped in the site. Crosses: the particle is initially released 1 km below the CIR radius. It decays toward the Lindblad resonance (LIR) and then suffers a secular increase of eccentricity, see Fig. 20. No trapping in the corotation site is observed in this case.

et al. 1993, Weidenshilling and Jackson 1993). Namely,

$$e(t) \sim \sqrt{4\alpha_\odot t/5|m|} \sim \sqrt{3.21 \times 10^{-8}\beta_\odot t_{\rm years}} \qquad (27)$$

when e is small.

Example of such captures are shown in Fig. 21. Two particles with $\beta_\odot = 0.57$ are released at $\Delta a = +4$ and -1 km from the CIR radius, respectively. During their decay, they cross the LER radius, where they remain trapped. In the meantime, their eccentricity increases as expected from Eq. (27), see Fig. 20. This situation is not stable because the eccentricity keeps on increasing until some new equilibrium is reached, for a very high eccentricity, estimated to be $\sim \sqrt{2/5|m|} \sim 0.1$ (*Ibid.*). Before this happens, however, violent collisions with the arcs or the continuous ring are likely to remove the particles trapped in the LER.

9. COLLISIONS

One of the most puzzling problems about the arcs is their apparent robustness against collisions. Avoiding collisions can be achieved by placing all the particles in nested epicycles with the same semi-major axis, but with different eccentricities. Apart from the highly unstable nature of this configuration against collisions, this geometry is at contrast with observations.

First, the corotation sites are fully occupied by material, implying a dispersion of semi-major axes, $\Delta a = W_{\rm CI} \sim 0.5$ km (Eq. (9)). Second, the observed physical width of the arcs ($\sim$15 km from the ground-based observations) is quite larger than $\sim$0.5 km. This requires a gradient of eccentricity $a\Delta e/\Delta a$ across the arcs. This point is discussed by Porco *et al.* (1995) and in Section 5.1, where Eq. (11) was used to derive an expected value $a\Delta e/\Delta a \sim -16.3$, and thus a width of $W \sim 7$ km. This is still too small compared to the observed widths, $W \sim 15$ km quoted above.

A third point concerns collisions in the arcs. Even in the most favorable case where all the particles have at all times the forced eccentricity given by Eq. 11, the streamlines still cross near quadrature (see Fig. 2 of Goldreich *et al.* 1986 or Fig. 24 of Porco *et al.* 1995). The relative velocity of two particles having extreme semi-major axes differing by $\sim$0.5 km is then

$$\Delta v_{\rm r} \sim an\,\Delta e \sim 1.4\ {\rm m\ sec^{-1}}, \qquad (28)$$

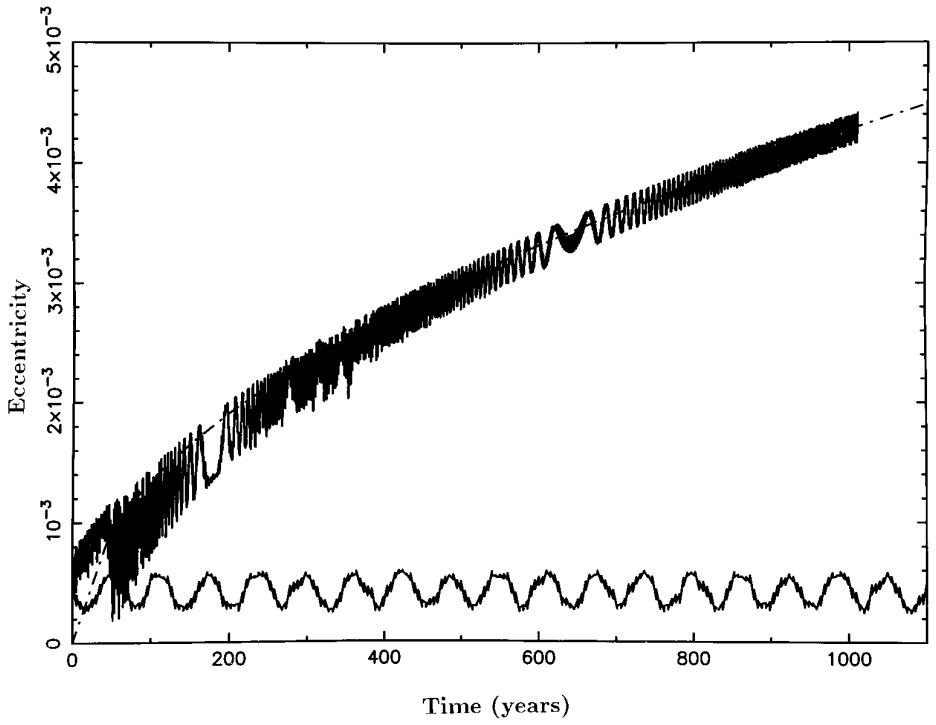

FIG. 20. Orbital eccentricities of the particles shown in Fig. 19 vs time. The lower curve shows the stable oscillations of the orbital eccentricity of the particle initially released in the corotation site. The upper curve illustrates how the eccentricity of the particle released just below the corotation site is pumped up by the LER. The dot–dashed curve shows the theoretical expected behavior of the eccentricity in this latter case (Eq. (27)).

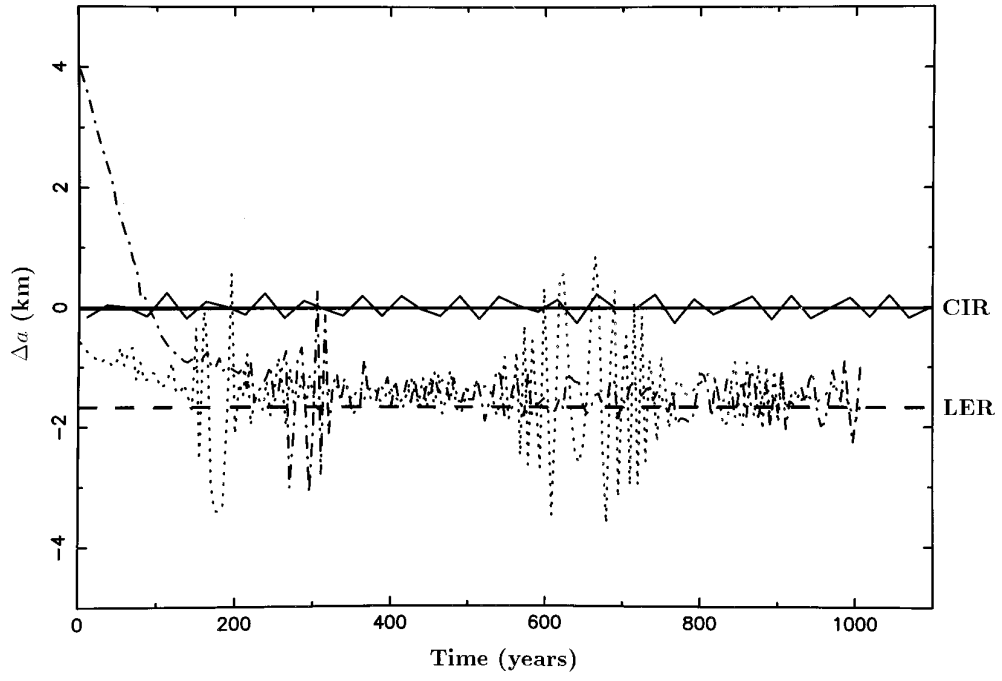

FIG. 21. Solid line: semi-major axes (with respect to the CIR radius) vs time of the particle shown as dots in Fig. 19. Dotted line: same, but for the particle shown as crosses in Fig. 19. A third integration (dot–dash line) is shown, corresponding to a particle initially released 4 km above the corotation site. Although the latter particles seem to be trapped at the LER resonance, they are not in a stable configuration, since their eccentricities keep on increasing, see Fig. 20.

where we used again $a\Delta e/\Delta a \sim -16.3$. The index r indicates that the relative preimpact velocity is essentially radial in this case.

This preimpact relative velocity Δv_r will cause a variation of both the longitudinal and radial velocities of the particles involved in the collision. The "worst case" (in the sense of the stability of the arcs) occurs for relatively elastic collisions, where a significant part of the energy of the collision may be redistributed in the longitudinal direction. This yields a variation of the longitudinal velocity $\Delta v_\theta \sim \Delta v_r \sim 1$ m sec^{-1} (where $v_\theta \sim an \sim 10.5$ km sec^{-1} is the tangential velocity of the arc particles). This implies a change in semi-major axis of

$$\Delta a \sim 2a \frac{v_\theta \Delta v_\theta}{(an)^2} \sim 10 \text{ km}, \tag{29}$$

a very large value, considering the narrowness of the corotation site (see also the discussion by Porco 1991).

A possibility to solve this problem is that the changes of velocity of both particles remain essentially radial, through a mechanism which should be explicited. When they collide near quadrature, the particles have a radial velocity of $v_r \sim ean$. Thus, a variation of the radial velocity on the order of $\Delta v_r \sim 1$ m sec^{-1} implies a variation of semi-major axis of

$$\Delta a \sim 2a \frac{v_r \Delta v_r}{(an)^2} \sim 5 \text{ m}, \tag{30}$$

which is now quite smaller than the width of the corotation site.

A further "improvement" can be achieved if the collisions are inelastic enough for the particles to damp completely their relative velocities (zero rebound coefficient). Then, the total energy lost during the collision is $\sim(\Delta v_r)^2/4$, implying a change in the semi-major axis of the system of the two particles

$$\Delta a \sim \frac{a}{2}\left(\frac{\Delta v_r}{an}\right)^2 \sim 0.25 \text{ m}, \tag{31}$$

an even safer value. The problem with that scenario is that it should lead to a rapid accretion of the particles in a few larger bodies. Thus, some disruptive (but not too catastrophic) mechanism is required to recreate smaller particles. Tidal forces could, for instance, do the job since the arcs are close to the Neptune's Roche limit.

A point worth being mentioned here is the stability of the libration motion in a corotation site, once the semi-major axis of the particle has been changed. As shown in Fig. 4 for a single particle, or in Figs. 11b and 12b for a collection of them, the libration motion *may* be stable even though the semi-major axis falls out of the $\sim$0.48-km-wide zone predicted by Eq. (7). As discussed in Section 5.2, this is due to the free eccentricity of the particles, which in turn can be caused by interparticle collisions. It is out of the scope of this paper to analyze the global effect of collisions on the arc stability, but this effect should be kept in mind when discussing the disruptive effect of collisions on the arcs. Recent results of collisional simulations of Neptune arcs are presented by Hänninen and Porco (1996), who show that meter-size and larger particles can actually be confined in a corotation site in spite of collisions.

10. DISCUSSION

We have studied in this paper the 3-D behavior of ring particles near a $m + 1{:}m$ mean motion resonance with a perturbing satellite on an inclined (but circular) orbit. Three resonances, acting together, define the long-term motion of the particles, namely the CIR, the LER, and the LIR. The oblateness of the planet causes slight differences in the radial locations of these resonances, in spite of the high value of $|m|$ (= 43 in the case of Adams ring). Consequently, the relevant resonant interactions of the particles and the satellite are found to occur in an interval of semi-major axes smaller than $\sim$2 km. The averaged motion of the particles is described by the system (3), where the strong couplings between the resonances stem from the smallness of j_p and j_n.

As long as the particle guiding centers remain close to the center of the corotation sites, with orbital eccentricities close to the eccentricity e_{forced} forced by the LER (Eq. (11)), then the particles remain stably trapped in corotation sites of azimuthal extension $360°/2m \sim 4.18°$ each.

The complexity of the motion appears rapidly, however, as one gets away from that ideal situation. In effect, the eccentricity gradient forced by the LER across the corotation site results in potential collisions with typical relative velocities on the order of 1 m sec^{-1}. This in turn kicks the particles outside the site, or for the least, drives them into quite complicated motions inside the arc. See, for instance, Fig. 4, where the particle semi-major axis explores a region 2 km wide and can reach the unstable points at $\Psi_{CI} = 0°$ or 360°, and yet remain stably trapped in the site.

We have shown that the coupling between the horizontal and the vertical motions is instrumental for driving the particle into a chaotic motion, tossing stochastically the particle from site to site, see Figs. 6 and 9. The migration from one site to the other occurs when the mutual inclination between the arc and the satellite is the smallest. This configuration happens every 30 years or so and is driven by the small, but not zero, differential nodal precession rate of the satellite and the particle. This modulation has important effects as to the aspect of the arcs at different moments; compare, for instance, the azimuthal profiles in

Figs. 11c and 12c, taken 50 years apart. If left alone, and even without any dissipative processes, the initial arc is scattered along the whole orbit in a few thousands years at most. See, for instance, Fig. 16, showing the azimuthal profile of a ring after 500 years, with an initial velocity dispersion between the 10^4 particles as low as 1 cm sec^{-1}.

The solar pressure of radiation will furthermore sweep out from the arcs, in a matter of decades, all the particles with a $\beta_\odot$ (ratio of the pressure of radiation to the solar gravitation) larger than $\sim$0.01, see Fig. 18. This corresponds to particles of size $s \lesssim 50$ μm for icy particle, in the limit of geometrical optics.

The results presented above seem to point toward the impossibility of maintaining ring arcs in the frame of the corotation resonance model. So, what is the status of such a model when confronted with the present arguments? The answer may lie in the fact that we are seeing ephemereal structures. The problem is then to know whether these structures are frequent enough to be *statistically* observable over time spans of billions of years. Also, there should be enough material available for renewing these structures over such long periods. Finally, one should explain why arcs are *observed* at corotation resonances after all.

The dust that we observe in the arcs must come from larger particles embedded in Adams ring, which are too rarefied to be detected, and which release the dust through meteoroid impacts and interparticle collisions (Colwell and Esposito 1990). This population probably exists as a result of continuous meteoroid bombardment, disruption, and reaccretion (Colwell and Esposito 1992, 1993). These large particles, however, should be found *everywhere* in Adams ring region, i.e., not only in the corotation sites themselves, but also in the space between two adjacent $m + 1$:m resonances. Note in passing that even then the percentage of particles right inside a corotation site is not so small, since adjacent resonances are separated by only $\sim$23 km near the 62,932-km radius (Fig. 1). Considering that each corotation site has a width of $\sim$0.5 km, this percentage should amount to about 1%.

As shown by Figs. 19 and 21, the Poynting–Robertson drag has only a mild effect on dust particles *already inside* the corotation site, and which have the forced eccentricity $e_{\rm forced}$. It just shifts by a small fraction of a degree the longitude of the particles with respect to the center of the corotation site. This is no longer the case, however, for particles which escape the corotation site, or which are formed from the beginning outside the arc region. These particles fall rapidly onto the nearest LER (Fig. 21), where their eccentricity is equally rapidly pumped up (Fig. 20). In that sense, it is interesting to note that the corotation sites "protect" particles against a secular increase of eccentricity caused by the nearby LER.

If this model is correct, then a small number of large particles continuously provides the dust and small particles necessary to form new rings. Outside the corotation sites, these rings are rapidly washed out by Poynting–Robertson drag, on scales of decades or centuries only. Inside the corotation sites, a quasi-equilibrium can be reached for those dust particles which maintain an eccentricity close to the forced value $e_{\rm forced}$. Thus, and independent of the physical lifetime of the grains (e.g., against micrometeoroid bombardment), corotation sites may correspond to locations where particles statistically accumulate. The stochastic migration of the few fragments which are the source of this dust can then explain the present distribution of material observed in Neptune's arcs, see Fig. 17 and the accompanying discussion. For this scenario to be valid, the large particles must not suffer too frequent collisions between themselves, and this is the case if the large particles are not too numerous. The ultimate time scale over which arcs can be visible, as features concentrated in a limited longitude range, is then the time scale for complete spreading by stochastic diffusion, i.e., several thousand years according to our simulations.

We note that the total mass of Neptune's arcs would represent, if merged into a single satellite, a rather small body with a size certainly not larger than $\sim$1 km, and probably quite smaller (Sicardy and Lissauer 1992). In contrast, *Voyager* has found several satellites whose orbits are intertwined with Neptune's rings. For instance, if Larissa, Galatea, Despina, Thalassa, and Naiad are merged together, the resulting body would have a radius larger than $\sim$120 km (Smith *et al.* 1989). In other words, the bulk of material already contained in the known satellites represents several million times the present mass of the arcs. This can provide over time scales of a billion years the necessary source for ringlets of the type of Adams, each of them having a time life of some thousands years. In that sense, an individual arc would be a rather short-lived feature by solar system standards, but the chance to observe some of them at a corotation resonance and at a given moment would not be so meager.

A natural continuation of this work is of course the study of other arc structures, as observed for instance in Saturn's F ring, and the relation it bears with the satellites Pandora and Prometheus. Another direction to pursue, which was not considered here, is the influence of self-gravity in ringlets which orbit close to the Roche limit of the planet they circle (Canup and Esposito 1995). Corotation sites could be in this context preferential locations where ongoing accretion forms objects intermediate between particulate rings and compact satellites.

APPENDIX A: MEAN MOTION RESONANCES

Expansion of the Perturbing Potential

Considering the Keplerian motion as the unperturbed one, the particle is submitted to the perturbing potentials from (i) the satellite,

Φ_s, and (ii) the planet's oblateness, Φ_{J_2}. The perturbing potential of the satellite

$$\Phi_s = -GM_s\left[\frac{1}{|\mathbf{r}-\mathbf{r}_s|} - \frac{\mathbf{r}.\mathbf{r}_s}{r_s^3}\right], \tag{A1}$$

can be Fourier expanded in series containing trigonometric terms with arguments $(m + k + k_s)\lambda_s - m\lambda - k\tilde{\omega} - k_s\tilde{\omega}_s$ or $2[(m + l + l_s)\lambda_s - m\lambda - l\Omega - l_s\Omega_s]$, where the coefficients are all integers. We keep only the first-order terms in eccentricity and the second-order terms in inclination. This corresponds to first-order eccentric resonances, i.e., $k + k_s = 1$, and to second-order inclined resonances, i.e., $2(l + l_s) = 2$.

The Fourier expansion of Φ_s is straightforward, although rather tedious. The general technique is detailed in Brouwer and Clemence (1961), or in Shu (1984). A more specific expansion, applied to planetary arcs, can be found in Sicardy (1991).

On the other hand, the dominant term arising from the planet's oblateness reads

$$\Phi_{J_2} = \frac{GM_N}{r}J_2\left(\frac{R_N}{r}\right)^2 P_2(\cos\theta), \tag{A2}$$

where J_2 is the second zonal harmonic, r, θ, ϕ are the usual spherical coordinates, and P_2 is a Legendre polynomial. Other terms in J_4, J_6 could in principle be included. However, due to their smallness, they would not change the form of the equations of motion, nor the basic couplings between the resonances. These terms are considered, however, in Eqs. (A6) in order to derive accurately the locations of the resonances.

The expression for the perturbing function R (*opposite* of the perturbing potential) is then, to lowest possible orders in e, e_s, I, I_s, and J_2,

$$\begin{aligned} R = &-a_s n_s \frac{M_s}{M_N}[Ae\cos(\Psi_{LE}) + Ee_s\cos(\Psi_{CE})] \\ &+ a_s n_s \frac{M_s}{M_N} V\left[I^2\cos(\Psi_{LI}) + I_s^2\cos(\Psi_{CI}) \right. \\ &\left. - 2II_s\cos\left(\frac{\Psi_{LI}+\Psi_{CI}}{2}\right)\right] \\ &+ \frac{1}{2}a^2n^2J_2\left(\frac{R_N}{a}\right)^2\left(1-\frac{3}{2}e^2\right)\left(1-\frac{3}{2}I^2\right), \end{aligned} \tag{A3}$$

where Ψ_{LE}, Ψ_{CE}, Ψ_{LI}, and Ψ_{CI} are the four resonant angles defined in Table II. The coefficients A, E, and V are combinations of Laplace coefficients $b_\gamma^{(m)}$

$$\begin{aligned} A &\equiv \frac{1}{2}\left[2(m+1)b_{1/2}^{(m+1)} + \alpha\frac{db_{1/2}^{(m+1)}}{d\alpha}\right] \\ E &\equiv \frac{1}{2}\left[(2m+1)b_{1/2}^{(m)} + \alpha\frac{db_{1/2}^{(m)}}{d\alpha}\right] \\ V &\equiv \frac{1}{8}\alpha b_{3/2}^{(2m+1)}, \end{aligned} \tag{A4}$$

where α stands for a/a_s. For order of magnitude considerations, it is useful to note that A and $-E$ are of order m, and that V is of order m^2. For large $|m|$, we have $A/m \sim -E/m \sim 0.802$ and $V/m^2 \sim 0.085$.

From now on, we assume that the satellite has a circular orbit ($e_s = 0$, see the text). This leaves us with only three resonant angles Ψ_{LE}, Ψ_{CI}, and Ψ_{LI}. The problem is then simplified, but it keeps nevertheless its 3-D aspect, and in particular, the couplings between the horizontal and the vertical resonances.

Rates of Change of the Orbital Elements

The variations of the particle's orbital elements are derived from the total averaged Hamiltonian $\mathscr{H}$

$$\mathscr{H} = \frac{GM_N}{2a} + R - \Lambda, \tag{A5}$$

where the action Λ is the conjugate of the time (Brouwer and Clemence 1961).

The equations are simplified if we choose for the origin of the semi-major axes the radius a_{CI} corresponding to the inclined corotation resonance. This is the most natural origin for semi-major axes, since the arcs are in principle confined near this radius.

The averaged Hamiltonian $\mathscr{H}$ can then be expressed in terms of the quantities χ, Ψ_{CI}, h, k, u, v, u_s, and v_s defined in Eqs. (1), in the main text. The calculation of the rates of change of the first six quantities is then a matter of lengthy, but straightforward algebra (Brouwer and Clemence 1961), yielding the system (3) in the main text.

Location of the Resonances

The absolute geometrical radius of a resonance can be found from the condition $\dot{\Psi} = 0$, where Ψ is any of the resonant angles of Table II.

For instance, to find the radius of the LER, one must fix $\dot{\Psi}_{LE} = (m + 1)n_s - mn - \dot{\tilde{\omega}} = 0$. We know n_s from the Voyager observations (see Table I), and we can relate the mean motion n and the precession rate $\dot{\tilde{\omega}}$ of the particle to its geometrical radius a and to the planet's gravitational moments. Then one can solve for a. We have used the following relations between the mean motion, precession rates, and geometrical radius (Nicholson and Porco 1988, Borderies-Rappaport and Longaretti 1994)

$$\begin{aligned} n &= \left(\frac{GM_N}{a^3}\right)^{1/2}\left[1 + \frac{3}{4}\left(\frac{R_N}{a}\right)^2 J_2 - \frac{9}{32}\left(\frac{R_N}{a}\right)^4 J_2^2 - \frac{15}{16}\left(\frac{R_N}{a}\right)^4 J_4\right] \\ \dot{\Omega} &= \left(\frac{GM_N}{a^3}\right)^{1/2}\left[-\frac{3}{2}\left(\frac{R_N}{a}\right)^2 J_2 + \frac{9}{4}\left(\frac{R_N}{a}\right)^4 J_2^2 + \frac{15}{4}\left(\frac{R_N}{a}\right)^4 J_4\right] \\ \dot{\tilde{\omega}} &= \left(\frac{GM_N}{a^3}\right)^{1/2}\left[+\frac{3}{2}\left(\frac{R_N}{a}\right)^2 J_2 - \frac{15}{4}\left(\frac{R_N}{a}\right)^4 J_4\right], \end{aligned} \tag{A6}$$

where J_2 and J_4 are given in Table I. The equation $(m + 1)n_s - mn - \dot{\tilde{\omega}} = 0$ is then solved iteratively for a, and similar procedures are used for the other resonances.

APPENDIX B: THE MAPPING

Hill's Equation

We seek the variations of the epicyclic elements of a test particle during a conjunction with a satellite. These variations are derived using the 3-D Hill equations of motion. We will not enter in the details of this derivation, extensively discussed elsewhere, see Hénon and Petit (1986), Nakazawa *et al.* (1989a,b), and Hasegawa and Nakazawa (1990). However, we also take into account the planet's oblateness in our model, which slightly changes some of the equations previously derived.

The position of the particle (x, y, z) is measured in a Cartesian frame $Oxyz$ centered on the planet. Oxy is the equatorial plane of the planet, Ox is directed toward the satellite, Oy is perpendicular to Ox, in the direction of motion, and Oz is aligned with the planet rotation axis. We define the variables $X \equiv (x - x_s)/R_H$, $Y \equiv (y - y_s)/R_H$, and $Z \equiv (z - z_s)/R_H$, where $R_H = a_s H$ is the satellite Hill radius (Eq. (19)), and (x_s, y_s, z_s) is the satellite position. In the limiting case where M_s/M_N and $(a - a_s)/a_s$ tend to zero, the equations of motion for the particle relative to the satellite read

$$\begin{aligned} \ddot{X} &= [4n_0^2 - \mu_0^2]X + 2n_0\dot{Y} + F_X \\ \ddot{Y} &= -2n_0\dot{X} + F_Y \\ \ddot{Z} &= -\nu_0^2 Z + F_Z, \end{aligned} \tag{B1}$$

with

$$\mathbf{F} = (F_X, F_Y, F_Z) = -3fn_0^2\frac{\mathbf{\Delta}}{\Delta^3}, \tag{B2}$$

$\mathbf{\Delta} \equiv (X, Y, Z)$ and $f \equiv GM_N/a_0^3 n_0^2$. Note that the mass of the satellite does not appear in these equations (it is actually absorbed in R_H). The frequencies n_0, μ_0, and ν_0 are respectively the mean motion, the horizontal and vertical epicyclic frequencies in the satellite region. We also define the frequency ξ_0:

$$\xi_0 \equiv \frac{4n_0^2 - \mu_0^2}{3n_0}. \tag{B3}$$

In the Keplerian case, $n_0 = \mu_0 = \nu_0 = \xi_0$ and $f = 1$.

If the satellite has a zero mass ($\mathbf{F} = 0$), the general solution of (B1) is

$$\begin{aligned} X &= b - [p_1\cos(\mu_0 t) + p_2\sin(\mu_0 t)] \\ Y &= -\frac{3}{2}\xi_0 b(t - t_0) + 2\frac{n_0}{\mu_0}[p_1\sin(\mu_0 t) - p_2\cos(\mu_0 t)] \\ Z &= [q_1\sin(\nu_0 t) - q_2\cos(\nu_0 t)] \end{aligned} \tag{B4}$$

$$\begin{aligned} \dot{X} &= \mu_0[p_1\sin(\mu_0 t) - p_2\cos(\mu_0 t)] \\ \dot{Y} &= -\frac{3}{2}\xi_0 b + 2n_0[p_1\cos(\mu_0 t) + p_2\sin(\mu_0 t)] \\ \dot{Z} &= \nu_0[q_1\cos(\nu_0 t) + q_2\sin(\nu_0 t)], \end{aligned} \tag{B5}$$

where b, t_0, p_1, p_2, q_1, and q_2 are constants of integration. Without loss of generality, the origin of time can be chosen at the moment of the conjunction, i.e., $t_0 = 0$.

Variations of the Epicyclic Elements

We define the *reduced, relative* eccentricity $\mathbf{p}^*$ and inclination $\mathbf{q}^*$ of the system satellite–particle as

$$\mathbf{p}^* \equiv p_1 + jp_2 = e^*\exp(j\mu_0 t_{\tilde{\omega}}) \tag{B6}$$

$$\mathbf{q}^* \equiv q_1 + jq_2 = i^*\exp(j\nu_0 t_\Omega), \tag{B7}$$

where e^* and i^* are called the reduced relative eccentricity and inclination and $j \equiv \sqrt{-1}$. $t_{\tilde{\omega}}$ is the time when the radial separation $x - x_s$ of the particle and the satellite is minimum (*relative* periapse). Similarly, t_Ω is the time when the particle crosses the satellite orbital plane in the ascending direction (*relative* node).

We finally define the usual complex eccentricity and inclination of the particle and satellite as

$$\mathbf{p} \equiv e\cdot\exp(j\tilde{\omega}) \tag{B8}$$

$$\mathbf{q} \equiv i\cdot\exp(j\Omega) \tag{B9}$$

$$\mathbf{p}_s \equiv e_s\cdot\exp(j\tilde{\omega}_s) \tag{B10}$$

$$\mathbf{q}_s \equiv i_s\cdot\exp(j\Omega_s). \tag{B11}$$

Considering that the integrated apsidal and nodal precessions are small during the time of interaction (i.e., during a conjunction), we have

$$\mathbf{p}^* = \frac{1}{H}[\mathbf{p} - \mathbf{p}_s]\exp(-j\lambda_c) \tag{B12}$$

$$\mathbf{q}^* = \frac{1}{H}[\mathbf{q} - \mathbf{q}_s]\exp(-j\lambda_c), \tag{B13}$$

where λ_c is the (common) longitude of the two bodies at conjunction.

When the force $\mathbf{F}$ is nonzero, Eqs. (B4) and (B5) still formally provide the solution of (B1), except that the quantities b, p_1, p_2, q_1, and q_2 are now *osculating* epicyclic elements. The system (B1) then admits an integral of motion called the Jacobi constant

$$J = \mu_0^2\frac{e^{*2}}{2} + \nu_0^2\frac{i^{*2}}{2} - \frac{3}{8}\mu_0^2\frac{\xi_0}{n_0}b^2 - \frac{3fn_0^2}{\Delta}, \tag{B14}$$

a generalization of the usual Jacobi constant of the Hill problem in the case of an oblate planet. We calculate only the variations of p_1, p_2, q_1, and q_2 over a conjunction, and the conservation of J then provides the variation of b.

The variations of p_1, p_2, q_1, and q_2 due to $\mathbf{F}$ are given, e.g., by Hasegawa and Nakazawa (1990) for the Keplerian case. We have slightly different expressions in the case of an oblate planet, i.e., to lowest order in $1/b = R_H/(a - a_s)$:

$$\begin{aligned} \Delta p_1 &= 0 \\ \Delta p_2 &= A\frac{b}{|b|^3} \\ \Delta q_1 &= B\frac{q_2}{|b|^3} \\ \Delta q_2 &= -C\frac{q_1}{|b|^3}, \end{aligned} \tag{B15}$$

with

$$\begin{aligned} A &\equiv f\left(\frac{n_0}{\xi_0}\right)^2\left[\frac{16}{3}\left(\frac{n_0}{\mu_0}\right)K_0\left(\frac{2\mu_0}{3\xi_0}\right) + \frac{8}{3}K_1\left(\frac{2\mu_0}{3\xi_0}\right)\right] \\ B &\equiv f\left(\frac{n_0}{\xi_0}\right)^2\left[2\left(\frac{\xi_0}{\nu_0}\right) + \frac{8}{3}K_1\left(\frac{4\nu_0}{3\xi_0}\right)\right] \\ C &\equiv f\left(\frac{n_0}{\xi_0}\right)^2\left[2\left(\frac{\xi_0}{\nu_0}\right) - \frac{8}{3}K_1\left(\frac{4\nu_0}{3\xi_0}\right)\right], \end{aligned} \tag{B16}$$

and where $K_l(z)$ are the modified Bessel functions. In the Keplerian case, $n_0 = \mu_0 = \nu_0 = \xi_0$ and $f = 1$, and we retrieve the results of Hasegawa and Nakazawa (1990), with $A = 8.71$ ..., $B = 2.94$ ..., $C = 1.05$....

Symplectic Mapping

The variations of p_1, p_2, q_1, q_2 can be given in a Hamiltonian form

$$\begin{aligned}\dot{p}_1 &= +\frac{1}{\mu_0}\frac{\partial \phi_s}{\partial p_2}\\ \dot{p}_2 &= -\frac{1}{\mu_0}\frac{\partial \phi_s}{\partial p_1}\\ \dot{q}_1 &= +\frac{1}{\nu_0}\frac{\partial \phi_s}{\partial q_2}\\ \dot{q}_2 &= -\frac{1}{\nu_0}\frac{\partial \phi_s}{\partial q_1},\end{aligned} \tag{B17}$$

where $\phi_s = -3fn_0^2/\Delta$ is the perturbing potential of the satellite. Thus, the flows of (p_1, p_2) and (q_1, q_2) are area-preserving.

The mapping (B15) is *not* area-preserving, even if higher order terms in $1/b$ are included, as in Hasegawa and Nakazawa (1990). To make the mapping area-preserving, we first note that for a narrow ring, the variations of semi-major axis over many conjunctions are very small with respect to the distance of the satellite, i.e., $\Delta b \ll b$. Typical values in the case of Adams ring are, for instance, $\Delta a \sim 0.5$ km, while $a - a_s \sim 980$ km, i.e., $\Delta b/b \sim 5 \times 10^{-4}$. Also, if the value of b does not suffer systematic drift during time, as for those particles trapped in the arcs, then it can be maintained to its initial value b_0 over the entire integration. The mapping $(p_1, p_2) \to (p_1 + \Delta p_1, p_2 + \Delta p_2)$ is then obviously area-preserving since it is just a translation.

This is not the case for the mapping $(q_1, q_2) \to (q_1 + \Delta q_1, q_2 + \Delta q_2)$. We thus look for a mapping of the form

$$\Delta q_1 = \quad B\frac{q_2}{|b_0|^3} + Dq_1 \tag{B18}$$

$$\Delta q_2 = -C\frac{q_1}{|b_0|^3} + Eq_2, \tag{B19}$$

where D and E are constants adjusted so that the Jacobian of the above mapping, $1 + D + E + DE + BC/|b_0|^6$, is unity. Among the infinity of solutions for D and E, we choose the smallest possible values, namely,

$$D = E = -\frac{BC/|b_0|^6}{1 + \sqrt{1 - BC/|b_0|^6}}. \tag{B20}$$

The final version of the mapping is thus

$$\begin{aligned}\Delta p_1 &= 0\\ \Delta p_2 &= A\frac{b}{|b_0|^3}\\ \Delta q_1 &= B\frac{q_2}{|b_0|^3} + Dq_1\\ \Delta q_2 &= -C\frac{q_1}{|b_0|^3} + Eq_2,\end{aligned} \tag{B21}$$

The added terms in D and E should be small, so that the corrected mapping is close to the original mapping. We have $B \sim 3$ and $C \sim 1$, and in the case of Galatea and Neptune, $M_s/M_N \approx 2.1 \times 10^{-8}$, $a_s \approx 61952$ km, and $a - a_s \approx 980$ km, so that $R_H \approx 119$ km and $b \approx 8.3$. Consequently, the terms in D and E represent respectively a fraction of $\sim 1.8 \times 10^{-3}$ and $\sim 3.6 \times 10^{-3}$ of the main terms. The validity of the mapping, and in particular its ability to reproduce the various resonance phase portrait, is examined in the text, see Section 6.

Implementation of the Mapping

Consider a ring particle in conjunction with the satellite at time t_c, at the common mean longitude λ_c. The various frequencies n_0, μ_0, ν_0, and ξ_0, the satellite's Hill's sphere radius R_H and the coefficients b_0, A, B, C, D, and E entering in the mapping can be calculated once for all from the particle epicyclic elements and from Eqs. (A6), (B16), and (B20). Then:

(1) We first calculate the complex eccentricities and inclinations of the particle and the satellite (Eqs. (B8)–(B11)), the reduced relative eccentricity $\mathbf{p}^*$ and inclination $\mathbf{q}^*$ (Eqs. (B6) and (B7)), and the reduced impact parameter b.

(2) We apply the mapping (B21) to $\mathbf{p}^*$ and $\mathbf{q}^*$ to get the new values $\mathbf{p}^{*\prime}$ and $\mathbf{q}^{*\prime}$.

(3) The new value of b is derived from the conservation of the Jacobi constant J (Eq. (B14)).

(4) The new complex eccentricity and inclination, and the new semi-major axis of the particle are then

$$\begin{aligned}\mathbf{p}' &= H\mathbf{p}^{*\prime}\exp(j\lambda_c) + \mathbf{p}_s\\ \mathbf{q}' &= H\mathbf{q}^{*\prime}\exp(j\lambda_c) + \mathbf{q}_s\\ a' &= a_s(1 + Hb').\end{aligned} \tag{B22}$$

(5) The common mean longitude λ_c' of the two bodies at the next conjunction is

$$\lambda_c' = \lambda_c + n'\,\Delta t, \tag{B23}$$

where

$$\Delta t = \frac{2\pi}{|n_s - n'|}. \tag{B24}$$

The satellite mean motion n_s is taken from the Voyager observations (Owen *et al.* 1991, and see Table II). The particle mean motion and precession rates are related to the geometric mean orbital radius a through Eqs. (A6). This provides the new values of $\tilde{\omega}$, Ω, $\tilde{\omega}_s$, and Ω_s at the next conjunction, and the code returns to step (1).

ACKNOWLEDGMENTS

We thank S. Ferraz-Mello, P. Goldreich, J. Laskar, D. Lazzaro, J. J. Lissauer, and M. R. Showalter for several discussions on the dynamical points raised in this paper. We also thank C. C. Porco, J. Hänninen, and an anonymous referee for improving the presentation and content of the paper. D.W.F. was supported by CAPES Grant 4811/88-11 of the Brazilian Education Ministry.

REFERENCES

BORDERIES-RAPPAPORT, N., AND P.-Y. LONGARETTI 1994. Test particle motion around an oblate planet. *Icarus* **107,** 129–141.

BROUWER, D., AND G. M. CLEMENCE 1961. *Methods of Celestial Mechanics*. Academic Press, New York.

BURNS, J. A., P. L. LAMY, AND S. SOTER 1979. Radiation forces on small particles in the solar system. *Icarus* **40,** 1–48 (BLS).

CANUP, R. M., AND L. W. ESPOSITO 1995. Accretion in the Roche zone: Co-existence of rings and ringmoons. *Icarus* **113,** 331–352.

COLWELL, J. E., AND L. W. ESPOSITO 1990. A model of dust production in the Neptune ring system. *Geophys. Res. Lett.* **17**(10), 1741–1744.

COLWELL, J. E., AND L. W. ESPOSITO 1992. Origins of the rings of Uranus and Neptune. 1. Statistics of satellite disruptions. *J Geophys. Res.* **97,** 10,227–10,241.

COLWELL, J. E., AND L. W. ESPOSITO 1993. Origins of the rings of Uranus and Neptune. 2. Initial conditions and ring moon populations. *J. Geophys. Res.* **98,** 7387–7401.

COVAULT, C. E., I. GLASS, R. G. FRENCH, AND J. ELLIOT 1986. The 7 and 25 June 1985 Neptune occultations: Constraints on the putative Neptune ''arcs.'' *Icarus* **67,** 126–133.

FERRARI, C., AND A. BRAHIC 1994. Azimuthal brightness asymmetries in planetary rings. *Icarus* **111,** 193–210.

FORYTA, D. W. 1993. *Etude numérique des anneaux planétaires. Application aux arcs de Neptune.* Thèse de Doctorat, Observatoire de Paris.

GOLDREICH, P. 1992. Puzzles and prospects in planetary ring dynamics. In *Chaos, Resonances and Collective Dynamical Phenomena in the Solar System* (S. Ferraz-Mello Ed.), pp. 65–73. Kluwer Academic, Dordrecht/Norwell, MA.

GOLDREICH, P., S. TREMAINE, AND N. BORDERIES 1986. Towards a theory for Neptune's arc rings. *Astron. J.* **92,** 490–494.

HAMILTON, D. P. 1993. Motion of dust in a planetary magnetosphere: orbit-averaged equations for oblateness, electromagnetic, and radiation forces with application to Saturn's E ring. *Icarus* **101,** 244–264.

HÄNNINEN, J., AND C. PORCO 1996. Collisional simulations of Neptune's ring arcs. *Icarus,* submitted.

HASEGAWA, M., AND K. NAKAZAWA 1990. Distant encounters between Keplerian particles. *Astron. Astrophys.* **227,** 619–627.

HÉNON, M., AND J.-M. PETIT 1986. Series expansions for the encounter-type solutions of Hill's problem. *Celest. Mech.* **38,** 67–100.

HORANYI, M., AND C. C. PORCO 1993. Where exactly are the arcs of Neptune? *Icarus* **106,** 525–535.

HUBBARD, W. B., A. BRAHIC, B. SICARDY, L. R. ELICER, F. ROQUES, AND F. VILAS 1986. Occultation detection of a neptunian ring-like arc. *Nature* **319,** 636–640.

KOLVOORD, R. A., AND J. A. BURNS 1992. Three dimensional perturbations of particles in a narrow planetary ring. *Icarus* **95,** 253–264.

LIN, D. N. C., J. C. B. PAPALOIZOU, AND S. D. RUDEN 1987. On the confinement of planetary arcs. *Mon. Not. R. Astron. Soc.* **227,** 75–95.

LISSAUER, J. J. 1985. Shepherding model for Neptune's arc ring. *Nature* **318,** 544–545.

LISSAUER, J. J., AND P. D. NICHOLSON 1990. Models of Neptune's arc rings. *Adv. Space Res.* **10**(1), 231–237.

MIGNARD F. 1982. Radiation pressure and dust particle dynamics. *Icarus* **49,** 347–366.

MIGNARD, F. 1984. Effects of radiation forces on dust particles in planetary rings. In *Planetary Rings* (R. Greenberg and A. Brahic Eds.), pp. 333–366. Univ. of Arizona Press, Tucson.

MIGNARD, F., AND M. HÉNON 1984. About an unsuspected integrable problem. *Celest. Mech.* **33,** 239–250.

NAKAZAWA, K., S. IDA, AND Y. NAKAGAWA 1989a. Collisional probability of planetesimals revolving in the solar gravitational field. I. Basic formulation. *Astron. Astrophys.* **220,** 293–300.

NAKAZAWA, K., S. IDA, AND Y. NAKAGAWA 1989b. Collisional probability of planetesimals revolving in the solar gravitational field. II. The validity of the two-problem approximation. *Astron. Astrophys.* **221,** 342–347.

NICHOLSON, P. D., AND C. C. PORCO 1988. A new constraint on Saturn's zonal gravity harmonics supplied by *Voyager* observations of an eccentric ringlet. *J. Geophys. Res.* **93,** 10,209–10,224.

NICHOLSON, P. D., I. MOSQUEIRA, AND K. MATTHEWS 1995. Stellar occultation observations of Neptune's rings: 1984–1988. *Icarus* **113,** 295–330.

NICHOLSON, P. D., M. L. COOKE, K. MATTHEWS, J. H. ELIAS, AND G. GILMORE 1990. Five stellar occultations by Neptune: Further observations of ring arcs. *Icarus* **87,** 1–39.

OWEN, W. M., Jr., R. M. VAUGHAN, AND S. P. SYNNOTT 1991. Orbits of the six new satellites of Neptune. *Astron. J.* **101,** 1511–1515.

PORCO, C. C. 1991. An explanation for Neptune's ring arcs. *Science* **253,** 995–1001.

PORCO, C. C., P. D. NICHOLSON, J. N. CUZZI, J. J. LISSAUER, AND L. W. ESPOSITO 1995. Neptune ring system. In *Neptune and Triton* (D. P. Cruikshank and M. S. Matthews, Eds.), pp. 703–804. Univ. of Arizona Press, Tucson.

SHOWALTER, M. R., AND J. A. BURNS 1982. A numerical study of Saturn's F-ring. *Icarus* **52,** 526–544.

SHOWALTER, M. R., AND J. N. CUZZI 1992. Structure and particle properties of Neptune's ring system. *Bull. Am. Astron. Soc.* **24,** 1029.

SHU, F. H. 1984. Waves in planetary rings. In *Planetary rings* (R. Greenberg and A. Brahic, Eds.), pp. 513–561. Univ. of Arizona Press, Tucson.

SICARDY, B. 1991. Numerical exploration of planetary arc dynamics. *Icarus* **89,** 197–219.

SICARDY, B., AND J. J. LISSAUER 1992. Dynamical models of the arcs in Neptune's 63K ring (1989N1R). *Adv. Space Res.* **12**(11), 81–95.

SICARDY, B., F. ROQUES, AND A. BRAHIC 1991. Neptune's rings, 1983–1989: Ground-based stellar occultations observations. I. Ring-like arc detection. *Icarus* **89,** 220–243.

SICARDY, B., C. BEAUGÉ, S. FERRAZ-MELLO, D. LAZZARO, AND F. ROQUES 1993. Capture of grains into resonances through Poynting–Robertson drag. *Celest. Mech.* **57,** 373–390.

SMITH, B. A., L. A. SODERBLOM, D. BANFIELD, C. BARNET, A. T. BASILEVSKY, R. F. BEEBE, K. BOLLINGER, J. M. BOYCE, A. BRAHIC, G. A. BRIGGS, R. H. BROWN, C. CHYBA, S. A. COLLINS, T. COLVIN, A. F. COOK II, D. CRISP, S. K. CROFT, D. CRUIKSHANK, J. N. CUZZI, G. E. DANIELSON, M. E. DAVIES, E. DE JONG, L. DONES, D. GODFREY, J. GOGUEN, I. GRENIER, V. R. HAEMMERLE, H. HAMMEL, C. J. HANSEN, C. P. HELFENSTEIN, C. HOWELL, G. E. HUNT, A. P. INGERSOLL, T. V. JOHNSON, J. KARGEL, R. KIRK, D. I. KUEHN, S. LIMAYE, H. MASURSKY, A. MCEWEN, D. MORRISON, T. OWEN, W. OWEN, J. B. POLLACK, C. C. PORCO, K. RAGES, P. ROGERS, D. RUDY, C. SAGAN, J. SCHWARTZ, E. M. SHOEMAKER, M. SHOWALTER, B. SICARDY, D. SIMONELLI, J. SPENCER, L. A. SROMOVSKY, C. STOKER, R. G. STROM, V. E. SUOMI, S. P. SYNOTT, R. J. TERRILE, P. THOMAS, W. R. THOMSON, A. VERBISCER, AND J. VEVERKA 1989. Voyager 2 at Neptune: Imaging Science results. *Science* **246,** 1422–1449.

WEIDENSCHILLING, S. J., AND A. A. JACKSON 1993. Orbital resonances and Poynting–Robertson drag. *Icarus* **104,** 244–254.